MEDICAL ROBOTS

Ferromagnetic soft continuum robots

Yoonho Kim[1], German A. Parada[1,2], Shengduo Liu[1], Xuanhe Zhao[1,3]*

Small-scale soft continuum robots capable of active steering and navigation in a remotely controllable manner hold great promise in diverse areas, particularly in medical applications. Existing continuum robots, however, are often limited to millimeter or centimeter scales due to miniaturization challenges inherent in conventional actuation mechanisms, such as pulling mechanical wires, inflating pneumatic or hydraulic chambers, or embedding rigid magnets for manipulation. In addition, the friction experienced by the continuum robots during navigation poses another challenge for their applications. Here, we present a submillimeter-scale, self-lubricating soft continuum robot with omnidirectional steering and navigating capabilities based on magnetic actuation, which are enabled by programming ferromagnetic domains in its soft body while growing hydrogel skin on its surface. The robot's body, composed of a homogeneous continuum of a soft polymer matrix with uniformly dispersed ferromagnetic microparticles, can be miniaturized below a few hundreds of micrometers in diameter, and the hydrogel skin reduces the friction by more than 10 times. We demonstrate the capability of navigating through complex and constrained environments, such as a tortuous cerebrovascular phantom with multiple aneurysms. We further demonstrate additional functionalities, such as steerable laser delivery through a functional core incorporated in the robot's body. Given their compact, self-contained actuation and intuitive manipulation, our ferromagnetic soft continuum robots may open avenues to minimally invasive robotic surgery for previously inaccessible lesions, thereby addressing challenges and unmet needs in healthcare.

INTRODUCTION

Small-scale soft continuum robots capable of navigating through complex and constrained environments hold promise for medical applications (1–3) across the human body (Fig. 1A). Several continuum robot concepts have been commercialized so far, offering a range of therapeutic and diagnostic procedures that are safer for patients owing to their minimally invasive nature (4–6). Surgeons benefit from remotely controlled continuum robots, which allow them to work away from the radiation source required for real-time imaging during operations (5, 6).

Despite these advantages, existing continuum robots are often limited to relatively large scales due to miniaturization challenges inherent in their conventional actuation mechanisms, such as pulling mechanical wires or controlling embedded rigid magnets for manipulation. Tendon-driven continuum robots (7–10) with antagonistic pairs of wires are difficult to scale down to submillimeter diameters due to increasing complexities in the fabrication process as the components become smaller (11–13). The miniaturization challenges have rendered even the most advanced form of commercialized continuum robots, mostly for cardiac and peripheral interventions (14), unsuited for neurosurgical applications due to the considerably smaller and more tortuous vascular structures (6). Magnetically steerable continuum robots (15–19) have also remained at large scale because of the finite size of the embedded magnets required to generate deflection under applied magnetic fields. Recently, a submillimeter-scale device (500 μm in diameter) with tiny magnets embedded in a soft polymer rod has been proposed for potential use in cardiac interventions, demonstrating magnetic steering and navigation in a coronary artery phantom (20, 21). However, navigating through cerebrovascular structures with fully soft-bodied continuum robots has not been realized so far. Furthermore, the inherent limitations associated with the use of such rigid magnets, particularly at submillimeter scale, are epitomized by the fact that several products of magnet-tipped microguidewires seeking U.S. Food and Drug Administration (FDA) premarket approval were later recalled because of the concern that tiny magnets at the tip could break off (22), which may lead to undesired clinical problems.

Recently, burgeoning efforts have been made to use soft-bodied robots in the medical domain, with great expectations for enhanced safety due to their inherent compliance (1, 3, 23, 24). Despite the purported advantage, the field of soft robotics is still faced with a set of key challenges. First, existing soft robots based on pneumatic or hydraulic actuations are mostly heavily tethered, which limits their use in realistic medical applications that typically require tether-free actuation (25). Second, most soft robots are difficult to accurately control based on quantitative models, largely because their actuation mechanisms often rely on highly nonlinear deformation or instabilities (26). Third, conventional soft robots are difficult to miniaturize below millimeter scales, because their fabrication schemes are often unfavorable to such small size (1, 27).

An emerging class of magnetically actuated soft robots, which we define as ferromagnetic soft robots, has recently been proposed (28–30) with great promise for biomedical applications, because they can potentially address the abovementioned limitations of conventional soft robots. They are composed of so-called ferromagnetic soft materials, in which magnetized or magnetizable microparticles are uniformly dispersed in soft polymeric matrices. Exploiting magnetic body torques and/or forces generated from the embedded particles under externally applied magnetic fields, ferromagnetic soft robots can be actuated remotely while at the same time controlled accurately based on quantitative models (28–30). Furthermore, the use of ferromagnetic microparticles as distributed actuation sources enables the miniaturization of ferromagnetic soft robots readily to submillimeter scales.

Further elaborating on the recent progress in materials, fabrication, and theory for ferromagnetic soft robots (28–31), we present

[1]Department of Mechanical Engineering, Massachusetts Institute of Technology, Cambridge, MA 02139, USA. [2]Department of Chemical Engineering, Massachusetts Institute of Technology, Cambridge, MA 02139, USA. [3]Department of Civil and Environmental Engineering, Massachusetts Institute of Technology, Cambridge, MA 02139, USA.
*Corresponding author. Email: zhaox@mit.edu
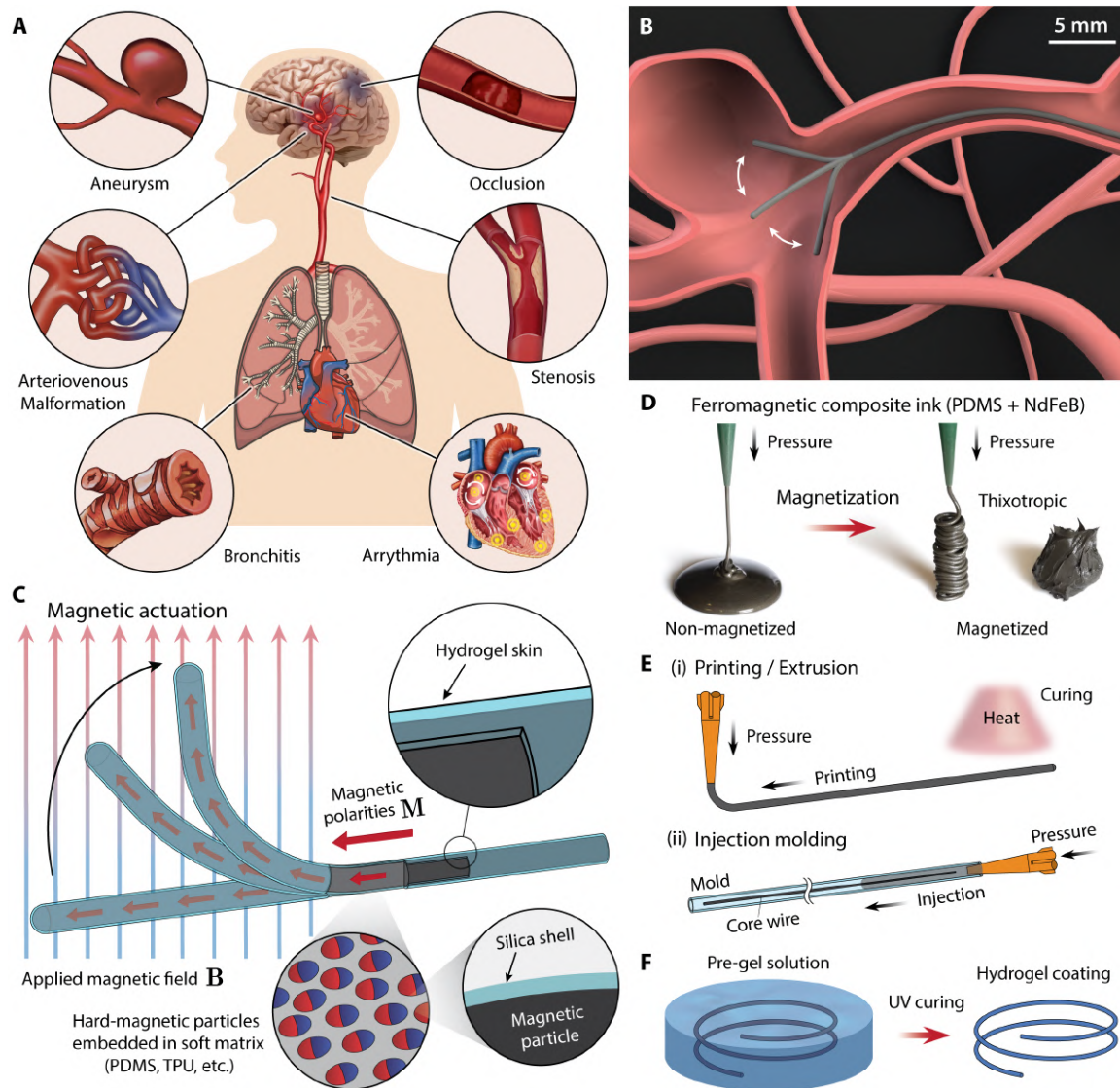
Fig. 1. Schematic illustration of ferromagnetic soft continuum robots with hydrogel skins. (**A**) Pathologic conditions in hard-to-reach areas across the human body where small-scale soft continuum robots with active steering and navigating capabilities have utility. (**B**) Illustration of the active steerability of a submillimeter-scale soft continuum robot navigating a complex vasculature with an aneurysm. (**C**) Schematic illustration of the magnetically responsive tip of the continuum robot with programmed magnetic polarities resulting from the hard magnetic particles embedded in the robot's body made of soft polymer matrix. The hydrogel skin provided a hydrated, self-lubricating layer on the robot's surface, and the silica shell coated around the embedded magnetic particles prevented their corrosion at the hydrated interface. (**D**) Ferromagnetic composite ink based on PDMS + NdFeB (20 volume %) before and after magnetization. When magnetized, the previously freely flowing ink became a thixotropic paste with shear yield stress due to the interaction between embedded magnetic particles. (**E**) Fabrication methods based on (i) printing/extrusion and (ii) injection molding. For printing, the magnetized ink was extruded through a micronozzle. For injection modeling, the ink was injected into a micromold in which a concentric functional core is placed. (**F**) Schematic illustration of hydrogel skin formation onto the outer surface of the fabricated ferromagnetic soft continuum robot.

submillimeter-scale ferromagnetic soft continuum robots that can navigate through highly constrained environments, such as narrow and tortuous vasculature, based on active, omnidirectional steering upon magnetic actuation (Fig. 1B). The robot's body is composed of soft polymer matrices with evenly dispersed hard magnetic micro-particles (Fig. 1C) and thus can be easily fabricated into submillimeter scale based on printing or injection molding (Fig. 1E). To cope with the substantial friction experienced while navigating highly unstructured environments (*5*, *32*), we grew hydrogel skin (*33*), a thin (10 to 25 μm) layer of hydrated cross-linked polymers, onto the robot's surface. This hydrogel skin effectively decreased the surface friction

due to its high water content. Enabled by the theoretical framework based on continuum mechanics developed for ferromagnetic soft materials (*31*), we also present our model-based material design strategies to optimize the actuation performance of our soft continuum robots. Combining all these features, we demonstrate the capability of navigating through complex and constrained environments, such as a cerebro-vascular phantom with multiple aneurysms, which are difficult to navigate with bulky robotic catheters or passive manual instruments. Incorporating a functional core in the robot's body, we further demonstrate additional functionalities, such as steerable laser delivery, in realistic in vitro environments with relevance to clinical challenges.

RESULTS

Ferromagnetic composite ink

Ferromagnetic materials in general develop strong induced magnetization under applied magnetic fields. Unlike soft magnetic materials, such as pure iron, which easily lose the induced magnetization once the external field is removed, hard magnetic materials, such as neodymium-iron-boron (NdFeB), are characterized by their ability to retain high remnant magnetization against the external field once they are magnetically saturated due to their high coercivity (fig. S1A) (31). The main body of our soft continuum robot was made of an elastomer composite that contains magnetizable microparticles (5-μm-sized on average; fig. S2C) of a NdFeB alloy (28–30). The soft polymer matrix of the robot's body was composed of either silicone [polydimethylsiloxane (PDMS)] or thermoplastic polyurethane (TPU) elastomers, depending on desired mechanical properties.

As the initial step of the fabrication process, our ferromagnetic composite ink was prepared by homogeneously mixing nonmagnetized NdFeB particles with uncured PDMS resin or TPU dissolved in solvent at a prescribed volume fraction. To impart desired rheological properties to the mixture for ease of fabrication later, we magnetized the whole mixture upon preparation by applying a strong impulse of magnetic fields to magnetically saturate the dispersed NdFeB particles. This turned the previously freely flowing mixture into a thixotropic paste (Fig. 1D) with shear-yielding (fig. S1B) and shear-thinning (fig. S1C) properties due to the strong interaction between the permanently magnetized NdFeB microparticles. The acquired rheological properties after magnetization were not only crucial for fabrication, as detailed in the following section, but also conducive to preventing phase separation of our composite ink due to sedimentation of the dispersed particles over time (fig. S1, D to F). The suppressed phase separation guaranteed microstructural uniformity (fig. S2B), which allowed us to postulate a homogeneous continuum when modeling the macroscopic behavior of our material to quantitatively predict the response of our soft continuum robot upon magnetic actuation (see the Supplementary Materials for details).

Printing/injection molding

The main body of our soft continuum robot consisted of a magnetically responsive tip (Fig. 1C) followed by a magnetically inactive segment (Fig. 4A). The soft continuum robot could be fabricated by either printing or injection molding, both of which required extruding the thixotropic paste–like ink through a micronozzle by applying pressure (Fig. 1E). The printing technique differs from conventional extrusion of molten thermoplastic polymers in that it did not require any heating to melt and fluidize the ink. The shear-thinning behavior of the magnetized ink ensured that the composite ink could be easily extruded when pressurized, and the presence of yield stress helped the deposited ink maintain its shape (30) instead of spreading and becoming flat (Fig. 1D). When additional mechanical support or functionalities were required, a functional core could be incorporated into the robot's body through the injection molding. For this process, a microtube was used as a mold, into which we injected the thixotropic composite ink while locating a concentric functional core inside the mold. Once the printing or injection was complete, the printed or molded ink underwent thermal curing (PDMS-based composite) or solvent evaporation (TPU-based composite) upon heating to solidify into the robot's body. During the heating process, the presence of yield stress helped the unsolidified ink maintain its shape on the printing substrate or remain stable in the mold instead

of flowing and escaping due to the decrease in viscosity at the elevated temperature. Thereafter, the magnetically active tip was uniformly magnetized again, along the axial direction, to have programmed magnetic polarities required to create deflection upon magnetic actuation (Fig. 1C).

Hydrogel skin

The hydrogel skin on the outer surface of the robot (Fig. 1C) consisted of cross-linked hydrophilic polymers [polydimethylacrylamide (PDMAA)] that were grafted onto the elastomer chains on the robot's surface. For the hydrogel coating procedure, we followed the previously reported protocol (33). First, the solidified robot's body was treated with an organic solution based on ethyl alcohol that contains hydrophobic photoinitiators (benzophenone). Exposure to this organic solution induced swelling-driven absorption of the photoinitiators into the robot's surface. The treated body was then immersed into a hydrogel monomer (DMAA) solution (Fig. 1F) containing hydrophilic photoinitiators (Irgacure 2959). Upon exposure to ultraviolet (UV) radiation (Fig. 1F), the hydrogel monomers were polymerized by the hydrophilic initiators while covalently grafted onto the surface-bound elastomers by the activated benzophenone, leaving a thin hydrogel-polymer interpenetrated layer on the surface. The thickness of the hydrogel skin was measured to be 10 to 25 μm from fluorescence microscope images taken from coated and uncoated samples with planar geometry (1-mm-thick sheet) (Fig. 2, A to D). The microscopic images identified the presence of the hydrogel skin on the coated samples.

The resulting hydrogel skin reduced the surface friction, which was characterized by the friction coefficients measured from a rheometer testing while applying different levels of shear rates and normal pressure (Fig. 2E). The measurements showed a 10-fold decrease in the friction coefficient (Fig. 2, H and I) as a result of the lubricious hydrogel skin in all given conditions. Furthermore, the coated hydrogel skin remained stable and undamaged even after prolonged shearing over an hour, exhibiting sufficient mechanical robustness (Fig. 2J). We also measured forces required to pull cylindrical specimens with and without hydrogel skin at a constant speed (200 mm min^{-1}) under different normal forces (2 and 5 N) applied by a pair of grips (Fig. 2F). The results showed a substantial decrease in the pulling force as a consequence of the self-lubricating hydrogel skin (Fig. 2G). When the applied normal force was 2 N, the hydrogel skin reduced the pulling force by a factor of 15 (from 2.65 to 0.18 N). As the normal force was increased from 2 to 5 N, the force required to pull the same uncoated specimen at the same rate increased by 150%. Compared with this, the required force to pull the coated specimen increased by only 60%, which illustrates how effectively the self-lubricating hydrogel skin reduces the surface friction under the increased load.

Silica shells around the particles

Ferromagnetic alloys have a highly corrosive nature due to the high content of iron. To prevent corrosion of the embedded NdFeB particles at the hydrated interface with the water-containing hydrogel skin, we coated the particles with a thin shell of silica (Fig. 1C) based on the condensation reaction of tetraethylorthosilicate (TEOS), which nucleated around the particles to form a cross-linked silica layer (fig. S2A). The resulting silica shell was identified to be 10 nm thick from transmission electron microscope (TEM) imaging (fig. S2D) and further verified by Fourier transform infrared spectroscopy, which indicated the presence of Si—O—Si bonds (fig. S2E). The effectiveness
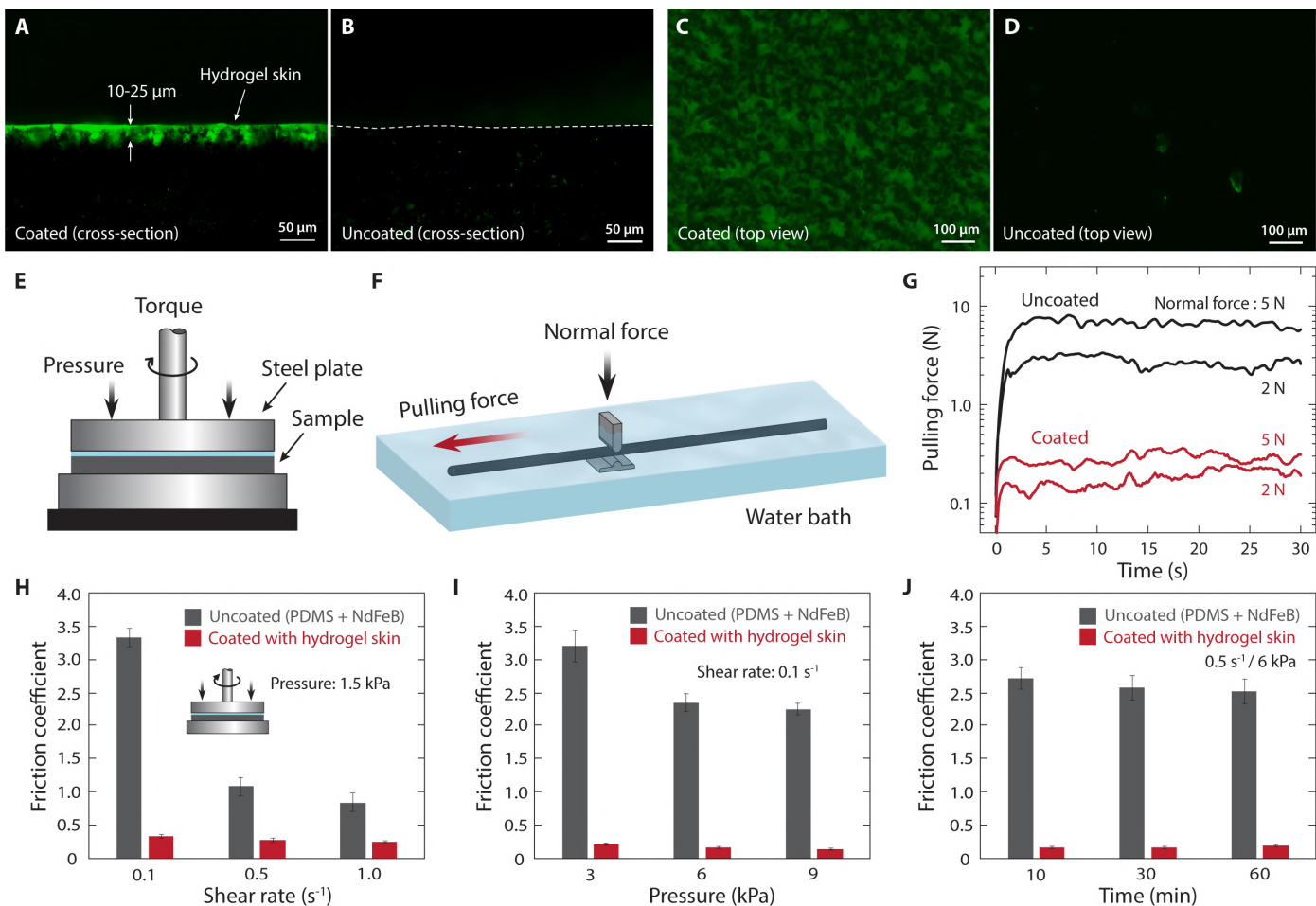
Fig. 2. Hydrogel skin as a lubricating layer. Cross-sectional views of (**A**) the coated specimen of PDMS + NdFeB (20 volume %) with hydrogel skin visualized by absorbed fluorescein and (**B**) the uncoated specimen without hydrogel skin. The dashed line in (B) indicates the boundary of the cross-section of the uncoated specimen. Top views of (**C**) the coated specimen with hydrogel skin and (**D**) the uncoated specimen. The fluorescing specks visible in the uncoated sample were due to residual fluorescein adsorbed onto the surface. (**E**) Schematic of testing setup for measuring friction coefficients using a rheometer. (**F**) Schematic of testing setup for measuring force required to pull a cylindrical specimen (diameter of 8 mm) at a constant speed under applied normal force by the pair of grips. (**G**) Semi-log plot of the pulling force measured over time during the pullout test performed at 200 mm min^{-1} for both coated and uncoated specimens under two different normal force conditions (2 and 5 N). Friction coefficients measured from both coated and uncoated samples under different (**H**) shear rates and (**I**) normal pressure. (**J**) Friction coefficients measured from prolonged shearing of both coated and uncoated samples up to 60 min at shear rate of 0.5 s^{-1} under normal pressure of 6 kPa. The error bars in (H) to (J) indicate the SDs of the mean values obtained from five different measurements.

of the silica shell in preventing the corrosion of NdFeB particles could be verified by performing a leaching test for both coated and uncoated particles with a weak acidic solution (0.2 mM HCl, pH 3). The results show highly oxidized uncoated particles but no visible change in silica-coated particles, which illustrates the anticorrosion effect of the silica shell formed around the NdFeB particles (fig. S2F). Because of the marginal thickness of the silica shell compared with the size of microparticles, the silica coating resulted in a slight increase in volume, which was roughly estimated to be around 1% when assuming a uniform silica layer around a spherical particle.

Design for optimal actuation

Both magnetic and mechanical properties of the robot's body made of ferromagnetic soft composites varied with the particle loading concentration. Here, we describe our material design strategy to optimize the actuation performance of the proposed ferromagnetic soft continuum robot. On the basis of our theoretical framework developed

for ferromagnetic soft materials (*30, 31*), we first provide the fundamental equations for quantitative description of the deformation of ferromagnetic soft materials upon magnetic actuation. We denote the magnetic moment density (or magnetization) at any point of a ferromagnetic soft material in the reference (undeformed) configuration by a vector $\mathbf{M}$. Under an applied magnetic field, denoted by a vector $\mathbf{B}$, the ferromagnetic soft material can deform. The deformation at any point of the material is characterized by the deformation gradient tensor $\mathbf{F}$. The application of the magnetic field on the embedded magnetic moment in the material generates the magnetic Cauchy stress $\boldsymbol{\sigma}^{\text{magnetic}} = -\mathbf{B} \otimes \mathbf{FM}$ that drives the deformation (*30, 31*), where the operation $\otimes$ denotes the dyadic product, which takes two vectors to yield a second-order tensor. Meanwhile, the deformation of the material generates the elastic Cauchy stress $\boldsymbol{\sigma}^{\text{elastic}}$, which is also a function of $\mathbf{F}$ defined by hyperelastic constitutive models such as the neo-Hookean model (*30, 31*). The total Cauchy stress in the material $\boldsymbol{\sigma} = \boldsymbol{\sigma}^{\text{elastic}} + \boldsymbol{\sigma}^{\text{magnetic}}$ is then substituted into the equilibrium

equation in eq. S3, from which the deformation (i.e., **F**) can be evaluated at every material point in equilibrium. Although alternate approaches based on magnetic body forces and torques have been proposed to calculate the deformation of ferromagnetic soft materials (28, 29), the current approach based on the magnetic stress can be readily implemented in commercial finite element software packages such as Abaqus. In addition, the magnetic stress can readily recover the magnetic body force and torque densities used in other approaches (see the Supplementary Materials for details).

Because the magnetically responsive tip of our soft continuum robot is axially magnetized (i.e., **M** along the axial direction), the tip tends to bend along the applied magnetic field **B** (Fig. 1C) due to the magnetic body torques generated from the embedded magnetized particles. To find the optimal particle concentration that yields the largest bending under given conditions and geometry, without loss of generality, we consider a beam of length L and diameter D under uniform magnetic field **B** that is being applied perpendicularly to **M** (Fig. 3A). In addition, to use a tractable analytical solution, we further assume that the magnetically active tip undergoes small bending, where the deflection (denoted δ in Fig. 3A) is below 10% of the tip length L. Then, we can reach the following analytical expression for the deflection of the magnetically active tip (details are available in the Supplementary Materials)

$$\frac{\delta}{L} = \frac{16}{9}\left(\frac{MB}{G}\right)\left(\frac{L}{D}\right)^2 \qquad (1)$$

where M and B are the magnitudes of the magnetization and the applied magnetic field, respectively, and G denotes the shear modulus of the material, which is considered as a neo-Hookean solid in the current analysis. Equation 1 relates the material properties (magnetization M and shear modulus G), geometry (beam length L and diameter D), and actuating field strength B to the normalized deflection. From Eq. 1, we notice that, for small bending, the deflection of the beam is linearly proportional to a dimensionless quantity, MB/G, while quadratically dependent on the aspect ratio L/D. The dimensionless quantity MB/G can be interpreted as the actuating field strength normalized by the material properties. Given that both M and G are dependent on the particle volume fraction, Eq. 1 implies that there will likely be an optimal point at which the normalized deflection is maximized.

The magnetization of the ferromagnetic soft composite is linearly proportional to the volume fraction of NdFeB particles (Fig. 3B) and hence can be expressed as

$$M = M_p \phi \qquad (2)$$

where M_p denotes the magnetization of the magnetic particles and ϕ denotes the particle volume fraction. Unlike the magnetization, the shear modulus increases nonlinearly as the particle concentration increases (Fig. 3C). This nonlinear dependence of shear modulus can be predicted by a simple analytical expression in Eq. 3, a so-called Mooney model (34), under the assumption that the increase in the shear modulus of particle-filled elastomer composites is analogous to the increase in the viscosity of particle suspensions (35)

$$G = G_o \exp\left(\frac{2.5\phi}{1 - 1.35\phi}\right) \qquad (3)$$

where G_o denotes the shear modulus of a pure elastomer with no particle. No significant difference was observed in both magnetization (Fig. 3B) and shear modulus (Fig. 3C) between the composite based on uncoated particles (PDMS + NdFeB) and the composite based on silica-coated particles (PDMS + NdFeB@SiO$_2$), which may be attributed to the marginal change in the particle volume due to the marginal thickness of the silica shell as discussed earlier. The small difference in shear modulus between the two types of composites also implies that the affinities of silicone elastomers with metal oxide (of uncoated particles) and silicon oxide (of silica-coated particles) surfaces are not substantially different.

By substituting Eqs. 2 and 3 into Eq. 1, we can identify the critical concentration ϕ_c at which the deflection is maximized for given conditions (field strength B and the geometric factor L/D). The critical volume fraction is calculated to be 0.207 (or 20.7 volume %), independent of M_p and G_o (Fig. 3D). Note that this critical concentration is obtained for small bending scenarios as described above. For large bending, the simulation and experimental results in Fig. 3E indicate that the actuation angle θ (defined in Fig. 3A) monotonically increases as a function of the normalized field strength MB/G for different aspect ratios L/D. Therefore, we can anticipate that the critical concentration predicted from the small-deflection analysis will remain effective for large bending cases as well. This is further validated by the simulation results for large bending presented in Fig. 3F, which show the actuation angle varying with the material composition and the applied field strength for a fixed geometry. The results indicate that the actuation angle reaches its maximum, for given applied field strengths, at the critical volume fraction (20.7 volume %) predicted above for the small bending case. As the applied field strength increases, however, the actuation angle begins to saturate while approaching 90°, making the curves around the peak flat (Fig. 3F).

When producing mechanical work out of magnetic actuation is of greater importance than the large deflection, we can optimize the actuation performance in terms of the energy density, which corresponds to the amount of work (per unit volume) that one can extract from the continuum robot. For small bending, the equivalent force generated at the free end of the beam can be calculated as $F = MBA$ (see the Supplementary Materials), where A denotes the cross-sectional area of the beam. Combining this with Eq. 1, we can find an analytical expression for the energy density u as follows

$$u = \frac{16}{9}\left(\frac{M^2 B^2}{G}\right)\left(\frac{L}{D}\right)^2 \qquad (4)$$

By substituting Eqs. 2 and 3 into Eq. 4, we find that the energy density reaches its maximum when the particle volume fraction is 29.3 volume % under given conditions in terms of applied field strength B and geometry L/D (Fig. 3G). This analytical prediction is validated by our model-based simulation for small bending (Fig. 3H), which shows how the energy density varies with the particle volume fraction when $B = 5$ mT and $L/D = 10$. As the bending becomes larger, however, the peak at which the energy density is maximized shifts to the right, toward the higher volume fractions (Fig. 3I). The peak eventually disappears when the actuation angle saturates, after which the energy density keeps increasing with the particle volume fraction. Qualitatively, this can be understood by considering the exponentially increasing stiffness (Fig. 3C), which dominantly contributes to the energy density when the deformation level remains almost unchanged (Fig. 3F).
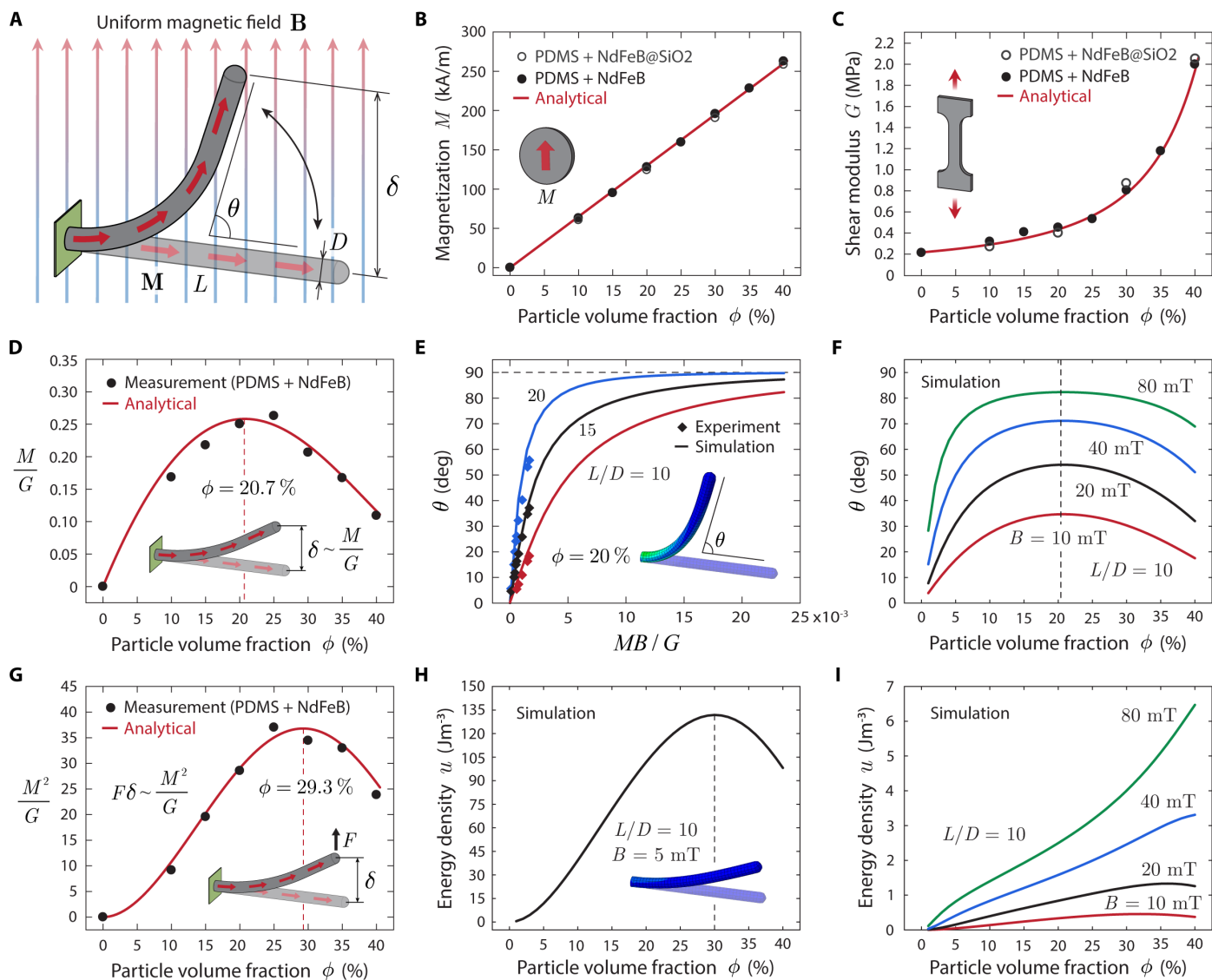
Fig. 3. Optimal design of ferromagnetic soft robot. (**A**) Schematic of the ferromagnetic soft continuum robot with uniform magnetization **M** along the axial direction deflecting toward the direction of the uniform magnetic field **B** applied perpendicularly to the body. The unconstrained length and the outer diameter of the robot are denoted L and D, respectively. δ indicates the deflection of the free end, and θ indicates the deflection angle. (**B**) Magnitude of magnetization, denoted M, linearly varying with the volume fraction of the embedded magnetic particles. (**C**) Shear modulus (denoted G) of the ferromagnetic composite at different particle concentrations. (**D**) Prediction of the variation of M/G, a characteristic quantity that determines the degree of deflection for small bending, with the particle volume fraction under given applied field strength for a given geometry. The unit of this quantity, T^{-1}, or equivalently $A \cdot m \, N^{-1}$, was intentionally omitted for simplicity. (**E**) Actuation angle predicted from finite element simulation and experimental measurements plotted against the applied field strength normalized by material properties (M and G) for a particular composition (20 volume %) with different aspect ratios: $L/D = 10, 15, 20$. (**F**) The variation of actuation angle with particle concentration at different actuation field strengths: $B = 10, 20, 40, 80$ mT, predicted from simulation results when $L/D = 10$. (**G**) Prediction of the variation of M^2/G, a quantity that characterizes the energy density in a deflected body for small bending case, with the particle volume fraction under given applied field strength for a given geometry. The unit of this quantity, A^2/N, was intentionally omitted for brevity. The average energy density predicted by finite element simulation for (**H**) small and (**I**) large bending cases, as a function of particle concentration.

When the material properties M and G are fixed because of a given particle volume fraction, the actuation performance of our ferromagnetic soft continuum robot under given applied field strength can still be optimized by adjusting the aspect ratio, according to Eqs. 1 and 4 along with the simulation results in Fig. 3. This implies that fine features with high aspect ratios, such as cilia-like soft continuum robots, would require significantly lower field strength to induce the bending actuation. Given that the printing-based method can easily produce very fine features, down to 80 μm in di-

ameter as demonstrated in the previous study (*30*), such extremely thin, cilia-like soft continuum robots may also be conceived for applications that require manipulating highly delicate structures. Despite these fabrication and miniaturization capabilities, however, we focused more on the design, fabrication, and demonstrations of our ferromagnetic soft continuum robots within the context of functional challenges and requirements for conventional continuum robots to constrain the scope of this study. Hence, our demonstrations are mostly focused on the functional capabilities achieved

from the proposed concept of ferromagnetic soft continuum robots—such as active steerability, navigability, and maneuverability—while suggesting additional possible functions enabled by the incorporated functional cores.

Active steering and navigation

Hereafter, we demonstrate the main capability of our ferromagnetic soft continuum robots designed for navigating complex and constrained environments, such as vasculature, based on active steering upon the magnetic actuation and additional functionalities enabled by the functional core incorporated in the robot's body. Figure 4A illustrates the proposed concept of a ferromagnetic soft continuum robot passing through a set of rings using its magnetically responsive tip, which follows the direction in which the actuating field is applied. For experimental demonstration, we used a cylindrical permanent magnet (diameter and height of 50 mm) to apply the actuating magnetic fields at a distance. The basic principle for magnetic actuation and steering was to align the central axis (denoted z axis in fig. S5A) of the magnet along the desired direction to induce bending of the robot's tip toward the desired direction (fig. S5B). Although the bending actuation in general is driven by magnetic body torques as discussed earlier, the spatial gradients of applied magnetic fields can also give rise to magnetic body forces, which further encourage the robot's tip to align itself along the magnet's central axis (fig. S6), as discussed in the Supplementary Materials.

Figure 4B and movie S1 show the experimental demonstration of the fabricated prototype, which selectively navigates through a set of loosely placed rings (see fig. S4A for details) based on steering achieved by manually manipulating a single magnet. The demonstrated prototype was fabricated through injection molding (Fig. 1E) of the PDMS + NdFeB composite ink and was designed to be 600 μm

in diameter. To provide mechanical support and pushability required for the demonstrated task, we incorporated a nickel-titanium alloy (nitinol) core in the robot's body (Fig. 4A). Because the nitinol core was from the tip of a commercial guidewire, the magnetically responsive tip was naturally connected to the commercial guidewire (see Materials and Methods for details). We also fabricated another prototype based on printed TPU + NdFeB composite without a core. The printed segment was also connected to the commercial guidewire. As demonstrated in fig. S3 and movie S2, the TPU-based prototype performed the same functional tasks shown with the PDMS-based prototype in Fig. 4B and movie S1. Because the printed segment does not contain any core for additional support, this prototype was designed to be thicker in diameter (810 μm) to ensure sufficient bending rigidity required for the demonstrated tasks. The navigating performance of the two prototypes is comparable when considering the average time taken to complete the demonstrated task: 50 ± 1.58 s with the first prototype and 54 ± 1.87 s with the second prototype. Given the higher degrees of freedom in terms of design and fabrication, we chose to use the PDMS-based composite for further exploration of possible designs and functionalities of the proposed ferromagnetic soft continuum robots with functional cores.

To enable making sharp turns and hence navigating through a tortuous path, we introduced a variation in the bending stiffness of the magnetically responsive part of our soft continuum robot. Now, the continuum robot (diameter of 600 μm) has a short (3-mm-long), softer segment at the distal end of the magnetically active portion. This softer segment was composed of the PDMS + NdFeB composite only and thus substantially softer than the remainder, which contained a stiff nitinol core (diameter of 80 μm). The effective Young's modulus of the stiffer segment (14 MPa) was calculated to be 10 times that of the softer segment (1.4 MPa) from Eq. 5 in Materials and
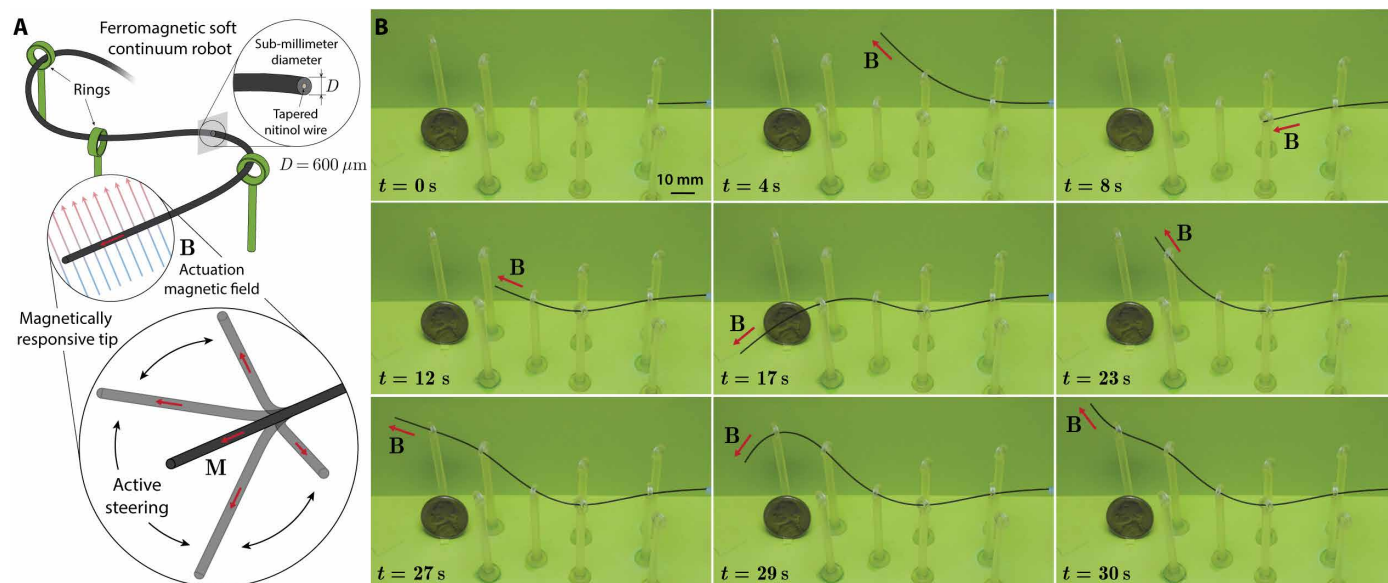
Fig. 4. Demonstration of active steering and navigating capabilities. (**A**) Schematic of the demonstrated ferromagnetic soft continuum robot with a magnetically responsive tip (with uniform magnetization **M**) and a tapered nitinol core required for active steering and navigation under magnetic actuation. (**B**) Experimental demonstration of the designed ferromagnetic soft continuum robot (based on PDMS + NdFeB composite) selectively navigating through a set of rings based on magnetic actuation and steering. The magnetic fields for actuation (20 to 80 mT) were generated by a cylindrical permanent magnet (diameter and height of 50 mm) at a distance (40 to 80 mm). The proximal end was pushed to advance the magnetically steered distal tip of the robot during the navigation. The outer diameter of the demonstrated prototype was 600 μm. Detailed dimensions of the demonstration setup are available in fig. S4A.

Methods. Both segments have uniform magnetization ($M = 128$ kA m^{-1}) along the axial direction. The softer and hence more responsive tip enables multiple modes and degrees of bending depending on the direction and strength of the applied actuating field, as well as the unconstrained length of the magnetically active segment, as predicted from our model-based simulation in Fig. 5 (A to C). When the unconstrained length of the stiff segment equaled that of the soft segment, only the very end tip of the continuum robot reacted effectively to the applied magnetic fields, creating a J-shaped tip (Fig. 5A). This is because the short unconstrained segment has a large bending stiffness due to the small aspect ratio, as predicted in Fig. 3E. As the unconstrained length increased, the bending stiffness of the stiffer segment decreased, which increased the radius of curvature of overall bending upon magnetic actuation (Fig. 5, B and C). Figure 5D and movie S3 show the experimental demonstration of our fabricated prototype navigating through a tortuous path formed by a series of tightly spaced rings (see fig. S4B for details) based on the ability to make sharp turns, which was enabled by the design described above.

To illustrate the potential impacts of the proposed ferromagnetic soft continuum robots in medical applications, we extended the demonstrated steering and navigating capabilities of our soft continuum robots to a more realistic, clinically relevant environment. To this end, we used a real-sized, silicone vascular phantom that replicates a particular cerebrovascular anatomy, called the circle of Willis, as well as the surrounding arteries with multiple aneurysms (localized dilation) at different locations. As can be seen in fig. S7, the vascular structures are highly complex and tortuous, involving several acute-angled corners. The inner diameter of the silicone vessels along the targeted path (from carotid artery to middle cerebral artery in fig. S7B) to be navigated by our continuum robot ranged from 2.5 to 7.5 mm, and the aneurysms to reach along the path were 9 mm (first), 7.5 mm (second), and 5 mm (third) in diameter (fig.

S7A). The overall distance navigated by the robot along the targeted path was around 250 mm (fig. S7, B and C). The required task for our ferromagnetic soft continuum robot was to reach all the aneurysms along the targeted path while demonstrating the ability to locate the robot's distal tip inside each aneurysm based on magnetic actuation and steering capabilities. In addition, direct contact of the robot with the inner wall of the aneurysms should be avoided, given that aneurysms have a high risk of rupture, which can lead to hemorrhagic stroke.

With the same prototype presented earlier (Fig. 5 and movie S3), we experimentally demonstrate the capability of our ferromagnetic soft continuum robot to successfully carry out the required tasks in the vascular phantom, which was filled with a blood analog that simulates the friction between commercial guidewires and real blood vessels. As can be seen in Fig. 6 and movie S4, the proposed ferromagnetic soft continuum robot was able to smoothly navigate through the targeted path while completing all the required tasks without any noticeable difficulties or unintended motion. The importance and the effectiveness of the self-lubricating hydrogel skin became evident when comparing the navigating performance of ferromagnetic soft continuum robots with and without the hydrogel skin. As shown in movie S5, the uncoated prototype suffered from the substantial friction acting on the robot while going through the first acute-angled corner, exhibiting unwanted jerky movement. Despite the omnidirectional steering capability that enabled the robot to orient its distal tip toward the desired direction, the significant friction did not allow the robot's body to proceed. Upon further pushing, followed by another jerk, the robot struck the inner wall of the first aneurysm. After hitting the second aneurysm in an unpredictable manner, the demonstrated prototype without hydrogel skin eventually failed to further proceed through the third acute and narrow corner.
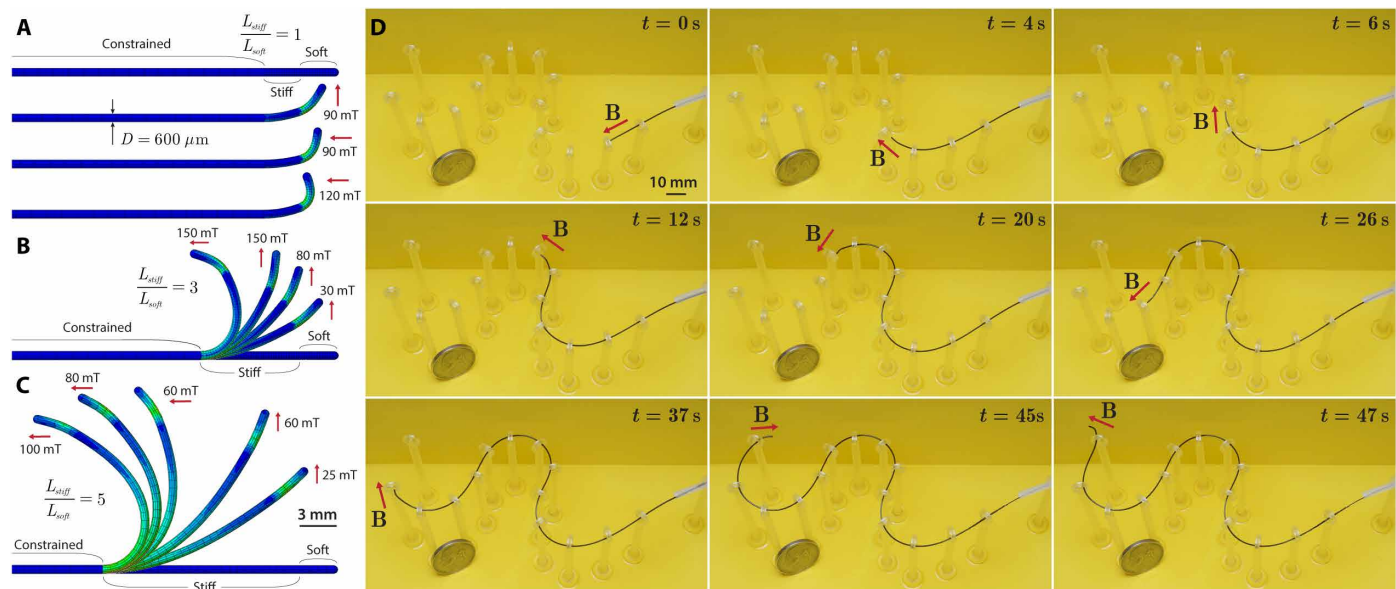
Fig. 5. Multiple modes and degrees of bending for navigating through a tortuous path. (**A** to **C**) Simulation results identifying multiple different modes and degrees of deflection, depending on the unconstrained length of the magnetically responsive tip (consisting of stiff and soft segments) as well as the applied field strength and direction, which help in creating sharp turns when navigating through tortuous paths. (**D**) Experimental demonstration of navigating through a highly nonlinear path formed by a set of tightly spaced multiple rings. The magnetic fields for actuation (20 to 80 mT) were generated by a cylindrical permanent magnet (diameter and height of 50 mm) at a distance (from 40 to 80 mm). The proximal end was pushed to advance the magnetically steered distal end of the robot during the navigation. The outer diameter of the demonstrated prototype was 600 μm. Detailed dimension of the demonstration setup is available in fig. S4B.
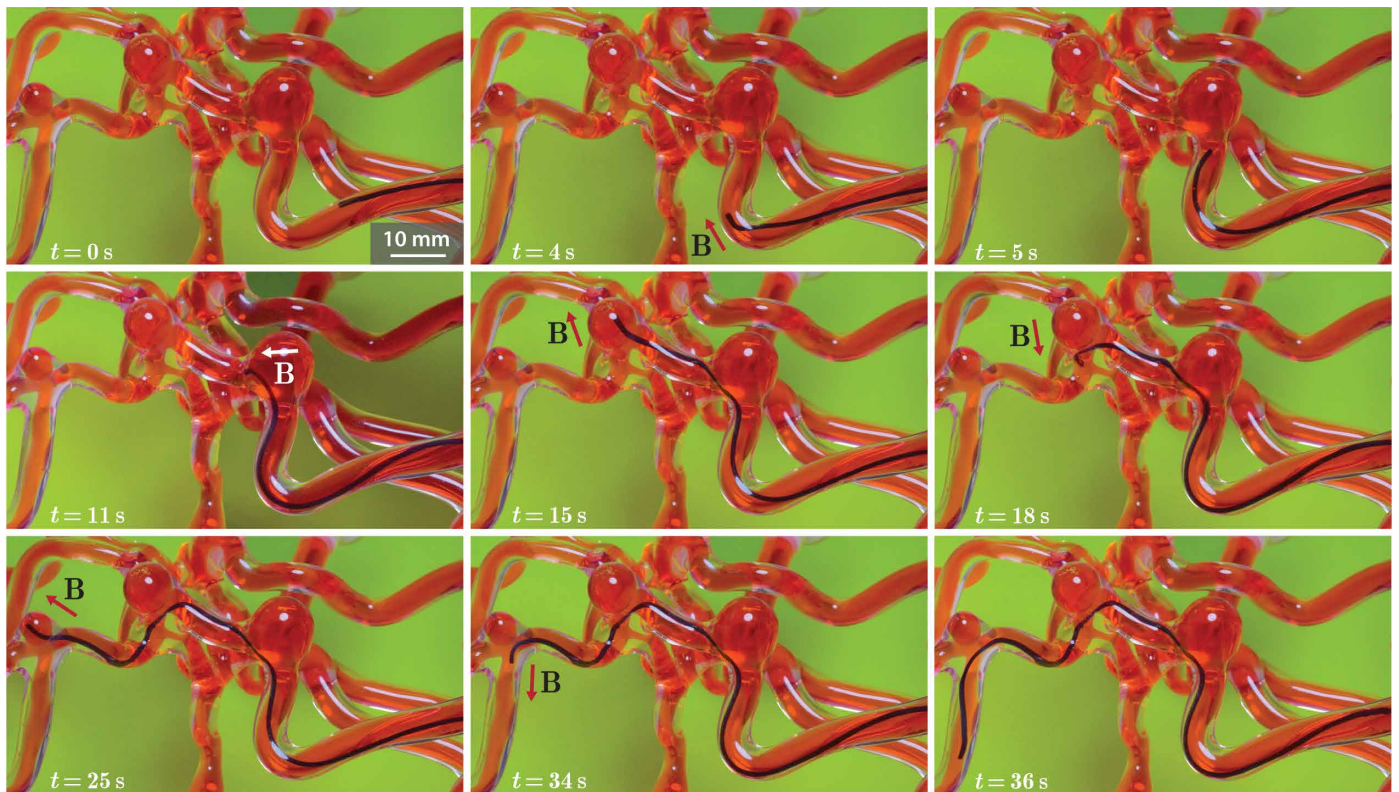
Fig. 6. Demonstration of navigating through a 3D cerebrovascular phantom network. The soft continuum robot first passed through the sharp corner with acute angulation (between $t = 0$ s and $t = 5$ s). The robot made another sharp turn after reaching the first aneurysm ($t = 11$ s) based on the magnetic steering capability to reach the second aneurysm ($t = 15$ s). Then, it made another sharp turn at the acute-angled corner beneath the second aneurysm ($t = 18$ s) to reach the third aneurysm ($t = 25$ s) and navigated further downstream ($t = 36$ s). Magnetic fields for actuation (20 to 80 mT) were generated by a cylindrical (diameter and height of 50 mm) permanent magnet at a distance (40 to 80 mm). The proximal end was pushed to advance the magnetically steered distal end of the robot during the navigation. The outer diameter of the demonstrated prototype was 600 μm. Note that the continuum robot may look thicker than the actual size due to the magnifying effect of the round, thick-walled silicone vessel. Detailed anatomy and dimensions of the phantom model are provided in fig. S7.

As discussed earlier, commercialized continuum robots with navigational capabilities are mostly limited to cardiac and pulmonary interventions, due mainly to the relatively large size (a few millimeters in diameter). Unlike those bulky devices, commercial guidewires can reach smaller and narrower areas, when carefully manipulated by skilled interventionalists, and hence are widely used in cerebrovascular and endovascular neurosurgery (6). For these manually controlled, passive guidewires, the distal tip of the device is typically preshaped with a fixed curvature or shapeable into curved or bent shapes, instead of being straight, for steering purposes (36, 37). This pre-bent distal tip can be oriented by manually twisting the proximal end of the device. After orienting the tip toward a desired direction through the twisting manipulation, the proximal end is pushed to advance the whole device forward. Upon this pushing manipulation, the floppy tip conforms to the environment and passively follows the continuous path as the guidewire moves forward.

To illustrate the importance of active steering capability of the proposed ferromagnetic soft continuum robots, we also compared the navigating performance of our prototype with that of a commercial guidewire with a comparable diameter in movie S6. We chose a preshaped hydrophilic guidewire with a fixed curvature that is large enough to cross the large gap within the first aneurysm. Note that, however, this demonstration with a certain preshaped device does not represent the guidewire manipulation performed by skilled inter-

ventionalists and therefore should be taken merely as an illustrative example. From the demonstration, we first notice that even though the pre-bent shape with large curvature enabled the device to pass the large (first) aneurysm almost effortlessly based on the twist-based steering, the very end tip of the device could act as an anchor that causes large friction and hence some jerky movements while navigating in a narrow vessel. In addition, the fixed curvature of the preshaped tip was not useful for the twist-based steering in highly constraining environments, such as the region near the third (smallest) aneurysm. Although the use of shapeable guidewires may alleviate this issue, additional time required for repetitive reshaping maneuvers and adjustments will likely be unavoidable (36). In this regard, we expect that the proposed soft continuum robot may overcome the current limitations of manual guidewires inherent in their passive steering mechanisms.

Steerable laser delivery

Further extending the demonstrated capabilities of the proposed concept of ferromagnetic soft continuum robots, we demonstrate additional functionalities enabled by a functional core. As an illustrative example with relevance to potential medical applications, we incorporated an optical fiber in the robot's body to demonstrate the concept of magnetically steerable laser delivery (Fig. 7A). Figure 7B shows the experimental settings for the demonstration and the fabricated
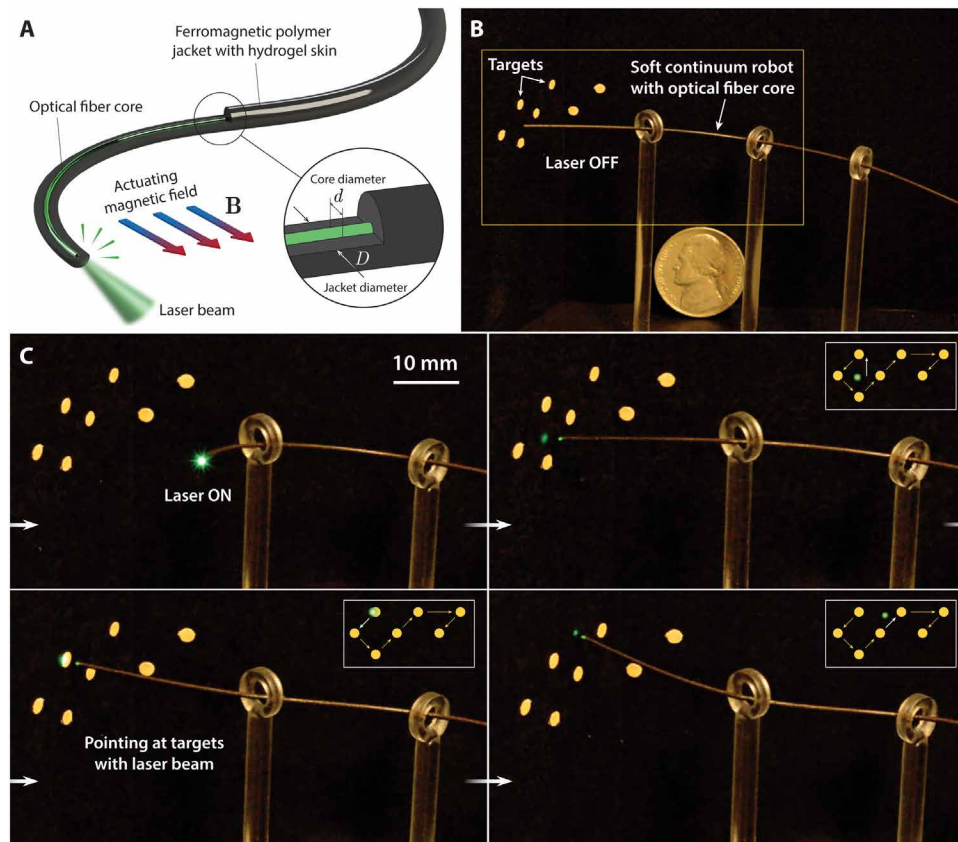
Fig. 7. Demonstration of steerable laser delivery. (**A**) Schematic illustration of the ferromagnetic soft continuum robot with an optical fiber, as a functional core incorporated in the robot's body, through which the laser is delivered. (**B**) Experimental setup for demonstrating steerable laser delivery. (**C**) Close view of the laser-emitting tip that accurately points at the small targets (2-mm dots) with the laser beam in a prescribed order based on omnidirectional magnetic steering. The magnetic fields for manipulation (20 to 80 mT) were generated by a cylindrical (diameter and height of 50 mm) permanent magnet at a distance (40 to 80 mm). The outer diameter of the demonstrated prototype is 500 μm.

prototype, whose outer diameter (denoted D in Fig. 7A) was designed to be 500 μm. The incorporated optical fiber with the outer diameter (denoted d in Fig. 7A) of 245 μm consists of a silica core, cladding, and protective acrylate coating. The given task was to accurately point at the small targets (2-mm dots) with the laser beam in a desired order based on the magnetic actuation (Fig. 7C). As shown in movie S7, the omnidirectional steering and the flexible motion allowed the soft continuum robot to successfully carry out the desired task.

One possible example of potential medical applications of this demonstrated capability may be laser-assisted treatment of vascular stenosis (or atherosclerosis; narrowing of an artery due to plaque buildup on the inner walls, as illustrated in Fig. 1A), which commonly occurs in the carotid artery, through which blood is supplied to the brain from the heart. As an illustrative example within this context, we demonstrate the proposed concept and functionalities of our laser-delivering soft continuum robot in the carotid artery section of the vascular phantom (fig. S7B), as shown in Fig. 8 and movie S8. In the demonstration, the continuum robot first reached the targeted site in the carotid artery and then emitted a green laser beam near the inner wall. It then changed the direction and the position of the laser-emitting tip using magnetic steering (Fig. 8A). After that, it turned off the laser and navigated downstream through the

carotid artery (Fig. 8B). The same prototype in Fig. 7 with a diameter of 500 μm was used for the current demonstration, and the inner diameter of the navigated carotid artery ranged from 5 to 7.5 mm.

However, the incorporation of an optical fiber, if not properly designed, can greatly increase the bending stiffness and may therefore limit the bending angle under given applied magnetic fields. The proof-of-concept prototype demonstrated above contained an unmodified optical fiber with a relatively thick protective acrylate coating. To reduce or eliminate the unnecessary portion of increased bending rigidity, this protective layer may be replaced with the ferromagnetic soft polymer jacket for further development. Once such design optimization is performed, the demonstrated capability to keep the laser-emitting tip in position based on magnetic steering may help in preventing unwanted motion or displacement of the tip from the desired location during the laser ablation, thereby improving the accuracy and the safety, which are of paramount importance throughout the whole procedure. There can be more possible applications. For instance, when equipped with a miniature complementary metal-oxide semiconductor (CMOS) sensor, while having multiple functional cores for both illumination and imaging, our soft continuum robots may further enable submillimeter-scale endoscopic procedures such as angioscopy (*38*) to better diagnose embolism (occlusion by a blood clot in Fig. 1A) in neurovasculature, which is far less accessible due to the considerably smaller size.

DISCUSSION

Here, we have introduced a class of submillimeter-scale soft continuum robots with omnidirectional steering capabilities upon magnetic actuation, based on ferromagnetic soft materials with programmed magnetic polarities in the robot's body. With a simple yet effective theoretical framework based on continuum mechanics, supported by our model-based finite element simulations, we have established a design strategy to optimize the actuation performance of the proposed ferromagnetic soft continuum robot. The hydrogel skin grown onto the robot's surface substantially reduced the friction and hence enabled navigation through complex and constrained environments such as tortuous and narrow phantom vasculature. Combined with these steering and navigating capabilities, additional functionalities such as steerable laser delivery were also demonstrated through the incorporation of an optical fiber as a functional core into the robot's body. Demonstrating these capabilities in realistic, clinically relevant environments in vitro, we have illustrated the applicability of ferromagnetic soft continuum robots for potential medical applications.
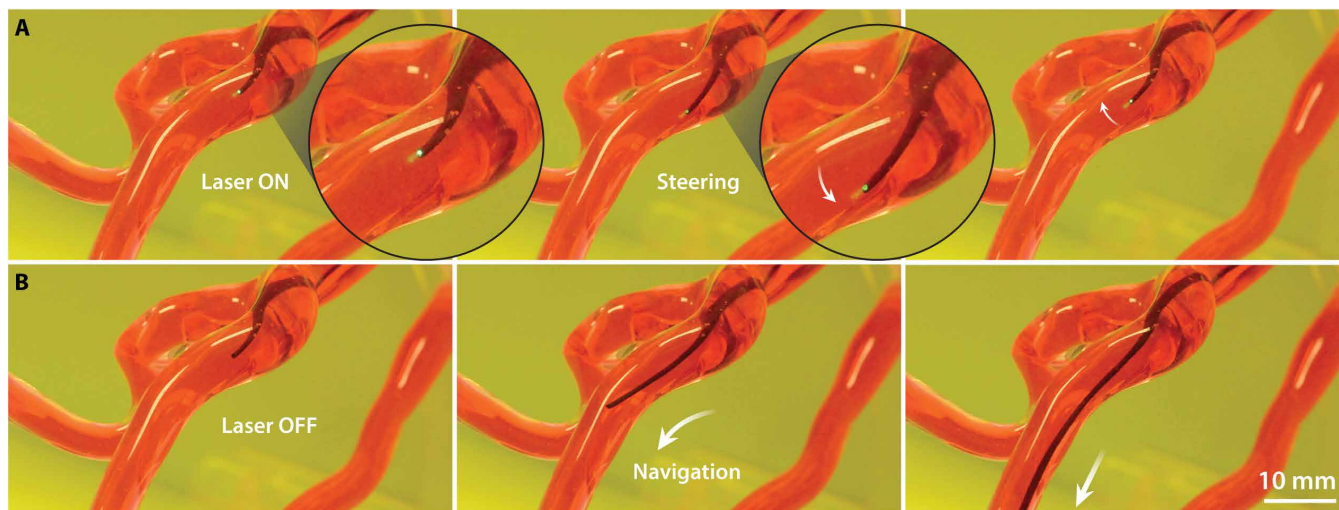
Fig. 8. Demonstration of steerable laser delivery in a phantom carotid artery. The ferromagnetic soft continuum robot (**A**) emitting a laser beam at different targeted sites in a phantom internal carotid artery (fig. S7B) based on magnetic steering and (**B**) navigating downstream after turning off the laser. The magnetic fields for manipulation (20 to 50 mT) were generated by a cylindrical (diameter and height of 50 mm) permanent magnet at a distance (50 to 80 mm). The proximal end was pushed to advance the robot during the navigation. The outer diameter of the demonstrated prototype is 500 μm. Again, the prototype may look greater than the actual size due to the magnifying effect of the round, thick-walled mock blood vessel.

For preclinical studies and clinical translation in the future, however, further studies will be required to evaluate the biocompatibility of our devices as external communicating, blood-contact, and short-duration (<24 hours) devices, according to relevant standards such as International Organization for Standardization (ISO) 10993-1 (Biological Evaluation of Medical Devices: Part 1). Although these tests have not been conducted in the current work, there is ample evidence that the materials used for the proposed devices would likely be biocompatible. First, both PDMS and TPU are known to be biocompatible with no acute cytotoxicity, as reported in a large volume of literature (*39*). The hydrogel skin, which encapsulates the robot's body, is also considered to be biocompatible, given that both PDMAA polymers and hydrogels have been reported to have no cytotoxicity (*40*, *41*). Although bare NdFeB materials are in general considered to be moderately cytotoxic due mainly to their highly corrosive nature, NdFeB magnets coated with noncorrosive metals or metallic alloys (e.g., tin, titanium, and nickel-copper) are known to be biocompatible and hence are widely used in orthodontic and orthopedic appliances (*42–44*). To prevent the corrosion, we have coated our NdFeB microparticles with silica, which is also known to be biocompatible and noncytotoxic (*45*, *46*). Because the particles were encapsulated in the silica shell, PDMS or TPU matrices, and hydrogel skin, we believe that the proposed ferromagnetic soft continuum robots would likely be biocompatible with no acute cytotoxicity; however, further studies are required to draw firmer conclusions.

There are a few limitations in the current study. First, the control of magnetic steering and navigation presented in the set of demonstrations was achieved under visual feedback with direct observation of states through the operator's eyes, which is not available when navigating deep inside the human body. In actual clinical settings, the state observation is enabled by fluoroscopic imaging, which visualizes radiopaque components or markers of guidewires/catheters in real time during navigation (*36*). Because our soft continuum robot contains a sufficient volume of radiopaque particles that are

visible under x-ray, the standard fluoroscopic imaging system will be directly applicable to enable visualization of the robot in actual clinical settings, which will be further investigated in future studies. Next, the magnetic steering demonstrated in the paper was achieved manually by adjusting the position and orientation of a single permanent magnet. To improve the accuracy and precision, existing magnetic manipulation systems (*15*, *47–50*) or more recent developments in omnidirectional and/or spatially selective magnetic field control (*17*, *18*, *21*, *51–53*) will need to be adopted for further translation of the proposed concept of ferromagnetic soft continuum robots.

If combined with these technologies, our ferromagnetic soft continuum robots may enable a range of minimally invasive interventional procedures that are currently unavailable with existing techniques. In particular, the ability to miniaturize our soft continuum robots down to the submillimeter scale, which is enabled by our materials and fabrication schemes, may enable access to hard-to-reach areas such as distal neurovasculature in a minimally invasive manner (*36*). Overall, the proposed concept of ferromagnetic soft continuum robots may open avenues to teleoperated, minimally invasive robotic surgery for previously inaccessible lesions, thereby addressing challenges and unmet needs in healthcare.

MATERIALS AND METHODS
Ferromagnetic composite ink preparation
The ferromagnetic composite ink was prepared by homogeneously mixing NdFeB microparticles with an average size of 5 μm (MQFP-B-2007609-089, Magnequench) into uncured PDMS resin (Sylgard 184, Dow Corning) or TPU (Elastollan Soft 35A 12P, BASF) dissolved [50 weight % (wt %)] in *N,N*-dimethylformamide (Sigma-Aldrich) at prescribed volume fraction using a planetary mixer (AR-100, Thinky) at 2000 rpm for 2 min. For PDMS-based ink, 5 wt % of curing agent containing platinum catalyst was added in the subsequent mixing for 45 s under the same condition, after cooling

down at room temperature for 1 min. The mixture was then magnetized by impulse magnetic fields (about 2.7 T) generated by an impulse magnetizer (IM-10-30, ASC Scientific) to impart magnetic polarities to the NdFeB particles embedded in the unsolidified elastomer resin.

Magnetic characterization

The magnetic moment densities of ferromagnetic soft composites based on PDMS + NdFeB with different particle concentrations were measured with a vibrating sample magnetometer (DMS 1660, ADE Technologies). Specimens were prepared from thin sheets of the composite materials obtained from molding by cutting them into 6-mm circles using a biopsy punch (Miltex Inc.) to fit into the sample holder of the magnetometer. The remnant magnetic moments of the samples were measured when the applied external field was zero and then divided by the sample volume to obtain the magnetization or magnetic moment density.

Mechanical testing

Rectangular planar sheets (12 mm by 35 mm by 1 mm) of ferromagnetic soft composites based on PDMS + NdFeB with different particle concentrations were prepared by molding and then cut into dog bone–shaped specimens with known dimensions (width, 4 mm; gauge length, 17 mm) for tensile testing. The specimens were tested on a mechanical testing machine (Z2.5, Zwick/Roell) with a 20-N load cell at a strain rate of $0.01 \ s^{-1}$. A nominal stress–stretch curve was plotted for each specimen, and the shear modulus was identified by fitting the experimental curve to a neo-Hookean model. When compared with the particle-filled elastomers, hydrogels were orders of magnitude softer in terms of Young's modulus. Because of this significantly lower modulus, the hydrogel skin does not contribute to the bulk mechanical property of the coated specimen, as reported in the literature (33). Therefore, for simplicity, the mechanical properties of the ferromagnetic soft composites were measured from uncoated samples without hydrogel skins.

Silica coating of magnetic particles

The NdFeB microparticles were coated with a layer of silica (SiO_2) through hydrolysis and polycondensation of TEOS (Sigma-Aldrich), widely known as the Stöber method, followed by the nucleation of the silica around the particle (fig. S1A). First, 40 g of NdFeB microparticles was dispersed in 1000 ml of ethanol while vigorously stirring to avoid sedimentation at 1500 rpm using a digital mixer (Cole-Parmer). Then, 60 ml of 29% ammonium hydroxide was slowly added to the mixture, followed by slow addition of 2 ml of TEOS. The mixture was stirred for 12 hours at room temperature and then washed with acetone multiple times after the reaction. The suspension was then vacuum-filtered to obtain the silica-coated particles.

Fabrication of ferromagnetic soft continuum robots

The TPU-based prototype demonstrated in fig. S3 and movie S2 was fabricated by joining a printed segment to a commercial guidewire with a TPU jacket and a nitinol core. For the printing process, the prepared composite ink based on TPU + NdFeB (30 volume %) was first loaded into a syringe barrel and then mounted to the custom-designed three-dimensional (3D) printer based on a Cartesian gantry system (AGS1000, Aerotech). A conical nozzle (outlet diameter of 838 μm, SmoothFlow Tapered Tip, Nordson EFD) was used to extrude the inks by applying pressure. The printed TPU composite

fiber was thermally welded to a commercial guidewire with a TPU jacket (ZIPwire Hydrophilic Guidewire; 810 μm diameter, Boston Scientific) using a heat shrink tube (inner diameter of 1.02 mm; Nordson Medical), in which the two segments were placed and locally heated at 190°C. During the heating localized at the junction, the TPU composites of both segments partially melted and then joined together when cooled, creating a seamless connection of the two segments.

The ferromagnetic soft continuum robots with functional cores presented in Figs. 4 to 8 were fabricated through injection molding, for which microtubes made of heat-resistant polymers, such as polytetrafluoroethylene or polyimide (Nordson Medical), were used as molds. For the prototypes presented in Figs. 4 to 6, in which tapered nitinol cores were incorporated, commercial guidewire products (Headliner Hydrophilic Guidewire; 300 μm diameter, Terumo) were used as templates. For a specified length of the commercial guidewire (25 cm from the distal tip), the TPU-based polymer jacket was first partially melted and stripped off by locally applying heat (250 to 300°C) to expose the tapered nitinol wire (distal diameter of 80 μm). Then, the prepared ferromagnetic composite ink based on PDMS + NdFeB (20 volume %) was injected into the 610-μm polyimide microtube through a conical nozzle (outlet diameter of 120 μm) while placing the tapered nitinol wire inside the mold (Fig. 1E). After curing upon heating at 160 to 190°C for 5 min, the mold tubing was stripped off with a razor blade to retrieve solidified body of the fabricated ferromagnetic soft continuum robot. For the prototype presented in Figs. 7 and 8, a single-mode optical fiber (diameter of 245 μm including the 3-μm core, 125-μm cladding, and protective acrylic polymer coating; Thorlabs Inc.) was used as a functional core, followed by the same injection molding procedures with 510-μm polyimide mold described above. After growing hydrogel skin on the outer surface (see below), all demonstrated prototypes were uniformly magnetized along the axial direction by applying an impulse magnetic field (about 2.7 T) generated by an impulse magnetizer (IM-10-30, ASC Scientific) to magnetically saturate the embedded NdFeB particles.

Hydrogel skin formation

Following the previously reported protocol (33), the uncoated samples were first cleaned with ethanol and isopropanol, followed by drying under nitrogen flow. To promote wettability of the uncoated polymer, we treated the samples with a plasma cleaner (PDC-001, Harrick Plasma) for 1.5 min. The plasma-treated samples were then immersed in an organic solution of ethanol containing 10 wt % benzophenone for 10 to 15 min. After removing excess solution on the surface with wipes, the samples were then immersed in a pre-gel solution containing 30 wt % hydrogel monomers (N,N'-dimethylacrylamide; DMAA, Sigma-Aldrich) and 1 wt % Irgacure 2959 (Sigma-Aldrich) based on deionized water, which was degassed for 5 min before preparing the pre-gel solution. For UV curing, the pre-gel solution bath was subjected to UV irradiation (CL-1000, UVP) for 60 min. Then, unreacted regents were removed by rinsing with deionized water using an orbital shaker (Microplate Shaker, VWR) for 24 hours. For imaging hydrogel skin (Fig. 2, A to D), both coated and uncoated samples (20 mm by 20 mm by 1 mm) based on PDMS + NdFeB (20 volume %) prepared by molding were immersed in an aqueous fluorescein solution before imaging to visualize the hydrogel layer.

Friction coefficient measurement

For friction coefficient measurement, both coated and uncoated samples (20 mm by 20 mm by 1 mm) were prepared based on

PDMS + NdFeB (20 volume %) composites. To quantify the friction coefficients, we measured the torque required to shear the specimens at prescribed shear rates (from 0.1 to 1.0 s^{-1}) under prescribed normal pressure (from 3 to 9 kPa) from a rotational rheometer (AR-G2, TA Instruments) in normal force control mode with a 20-mm-diameter steel plate geometry. Deionized water was smeared on top of both coated and uncoated surfaces before shearing the samples. The friction coefficients were calculated following the previously reported protocol (54).

Pulling test
For the pulling test, a cylindrical geometry was adopted for relevance to the actual shape of the continuum robot. For ease of measurement, however, the pulling test was conducted with a large-scale prototype with 8 mm diameter. Both coated and uncoated sheets of PDMS + NdFeB (20 volume %) composites with 1-mm thickness were wrapped around a glass rod with silicone adhesives (Sil-Poxy, Smooth-On Inc.) applied for secure bonding. The normal force was applied by a pair of half-cylindrical grips made of PDMS, where the upper grip was connected to the load cell of a mechanical testing machine (Z2.5, Zwick/Roell) to apply the prescribed normal force (2 or 5 N) to the specimen held between the grips. The specimens were pulled by a linear actuator equipped with a load cell at a constant speed (200 mm min^{-1}) while being immersed in a bath of deionized water. The load cell attached on the pulling grip measured the forces required to pull the specimens at the given speed.

Finite element analysis
For simulation results presented in Figs. 3 and 5, we used a user-defined element subroutine with the commercial finite element analysis software Abaqus. For parametric studies presented in Fig. 3 (F, H, and I), Eqs. 2 and 3 were implemented as input parameters for material properties. In all simulations, the bulk modulus was set to be 1000 times the shear modulus to approximate the incompressibility, and the direction and strength of a uniform magnetic field were defined as additional input parameters. For simulating multiple modes and degrees of bending presented in Fig. 5 (A to C), the magnetization parameter was defined as $M = 128$ kA m^{-1}, which was experimentally measured for samples of PDMS + NdFeB (20 volume %) composite. For the mechanical property of the softer segment, which is composed of the ferromagnetic elastomer composite only, the shear modulus value ($G = 455.6$ kPa) measured for PDMS + NdFeB (20 volume %) was used. Under the assumption of incompressible solids, for which $E \simeq 3G$, this shear modulus value is translated to Young's modulus of 1366.8 kPa. For the stiffer segment, which contains a 80-µm nitinol wire, the effective Young's modulus ($E_{eff} = 14{,}008$ kPa) was calculated from the following relation

$$E_{eff} = \left(E_{core} \left(\frac{d}{D} \right)^4 + E_{jacket} \left(1 - \left(\frac{d}{D} \right)^4 \right) \right) \quad (5)$$

where E_{core} and E_{jacket} denote the Young's moduli of the nitinol core and the ferromagnetic soft polymer jacket, respectively, whereas d and D denote the core and jacket diameter. For the nitinol core, the Young's modulus of the martensite phase (40 GPa) was used for the calculation. This calculation was validated by the good agreement between the simulation and experimental results presented in Fig. 3E.

Experimental validation of simulation results
For experimental validation of the model-based simulation results presented in Fig. 3E, we measured deflection angles from circular beam specimens (diameter of 600 µm) with different aspect ratios ($L/D = 10, 15, 20$) under uniform magnetic fields ranging from 5 to 60 mT generated by a pair of Helmholtz coils (10 cm diameter; MicroMagnetics). For each specimen, a nitinol core (diameter of 80 µm) was incorporated in the ferromagnetic soft polymer jacket based on PDMS + NdFeB (20 volume %) through the injection molding process described earlier to provide sufficient mechanical stiffness required to prevent gravitational sagging during the measurement. The incorporation of the stiff core resulted in 10-fold increase in the Young's modulus (and therefore the bending stiffness as well) as described above. Note that data were collected within a limited range because the maximum field strength (60 mT) generated from the Helmholtz coil used for the experiment was not sufficient to create full deflection. It is also worth noting that the limited range of experimental data does not mean possible deviation or disagreement between the experimental and simulation results at higher field intensities. The extensive validation on our model in the previous study (31) showed good agreement between the simulation and experimental results over the full range.

Magnetic actuation and demonstration
For all demonstrations presented in the paper, a cylindrical NdFeB magnet (diameter and height of 50 mm; DY0Y0-N52, K&J Magnetic Inc.) was used to apply magnetic fields required for actuation at distance. For magnetic steering and navigation, the direction and strength of the applied magnetic fields were varied by manually manipulating the magnet to change its position and orientation while advancing the proximal end of the template guidewire connected to the demonstrated ferromagnetic soft continuum robot. Detailed dimensions of the demonstration setups in Figs. 4 and 5 and movies S1 to S3—such as the location, height, and tilting angle of the rings—are provided in fig. S4. For the navigational tasks demonstrated in movies S1 to S4, each experiment was repeated five times to evaluate the average time taken for completion and the standard deviation. To avoid interoperator errors, one of the authors (Y.K.) performed the experiments. For demonstrations presented in Figs. 6 and 8 and movies S4 and S8, a commercially available cerebrovascular phantom model made of silicone (Trandomed 3D) was used along with a blood-mimicking fluid (Replicator Fluid, Vascular Simulations Inc.), which simulates the friction between commercial hydrophilic guidewire/catheter surfaces and the real blood vessels when used with a silicone vascular model. Further details on the cerebrovascular phantom model are provided in fig. S7. In these sets of demonstrations, the steering and navigating tasks were controlled with visual feedback by manually manipulating the position and orientation of a single permanent magnet while advancing the whole body by pushing the proximal end. The magnetic manipulation under spatially nonuniform fields exploited the magnetic body torques as the main source of actuation, as well as the magnetic body forces, which further helped the robot's tip to align itself toward the desired direction more effectively (more detailed discussions on the actuation mechanisms are available in Supplementary Text). For the steerable laser delivery demonstration presented in Figs. 7 and 8, we used a 3100-mW green light-emitting diode (530-nm wavelength; Thorlabs Inc.) as a light source.

SUPPLEMENTARY MATERIALS

robotics.sciencemag.org/cgi/content/full/4/33/eaax7329/DC1
Text
Fig. S1. Rheological properties of ferromagnetic composite inks.
Fig. S2. Characterizations of silica-coated magnetic particles.
Fig. S3. Experimental demonstration of active steering and navigating capabilities with a TPU-based prototype.
Fig. S4. Experimental setups and dimensions for the demonstrations of active steering and navigating capabilities of ferromagnetic soft continuum robots based on magnetic actuation.
Fig. S5. Magnetic actuation and steering mechanism based on a cylindral permanent magnet for experimental demonstrations of the proposed ferromagnetic soft continuum robots.
Fig. S6. Influence of spatial gradients of the actuating magnetic field on the actuation and steering of the ferromagnetic soft continuum robot.
Fig. S7. Dimensions and details of the cerebrovascular phantom model used for the experimental demonstration of the active steering and navigating capabilities of the proposed ferromagnetic soft continuum robot.
Movie S1. Demonstration of the ferromagnetic soft continuum robot actively steering and selectively navigating through a set of rings based on magnetic actuation.
Movie S2. Demonstration of the ferromagnetic soft continuum robot based on TPU + NdFeB (30 volume %) composite in the same experimental setup presented in movie S1.
Movie S3. Demonstration of the ferromagnetic soft continuum robot navigating through a highly nonlinear path formed by a set of tightly spaced multiple rings based on multiple modes and degrees of deflection upon magnetic actuation.
Movie S4. Demonstration of the ferromagnetic soft continuum robot with hydrogel skin (the same prototype presented in movie S3) navigating through a 3D cerebrovascular phantom (the circle of Willis model with multiple aneurysms).
Movie S5. Comparison of the navigating performance of the ferromagnetic soft continuum robot with (left) and without (right) hydrogel skin as a lubricating layer on the robots' surface in the same experimental setup presented in movie S4.
Movie S6. Comparison of the navigating performance of the ferromagnetic soft continuum robot with hydrogel skin (left) and a commercial hydrophilic guidewire with a preshaped tip (right).
Movie S7. Demonstration of the capability of steerable laser delivery with the ferromagnetic soft continuum robot with a concentric optical fiber incorporated as a functional core.
Movie S8. Demonstration of steerable laser delivery in the carotid artery of the vascular phantom model presented in movie S4.
References (55, 56)

REFERENCES AND NOTES

1. M. Cianchetti, C. Laschi, A. Menciassi, P. Dario, Biomedical applications of soft robotics. *Nat. Rev. Mater.* **3**, 143–153 (2018).
2. G.-Z. Yang, J. Bellingham, P. E. Dupont, P. Fischer, L. Floridi, R. Full, N. Jacobstein, V. Kumar, M. McNutt, R. Merrifield, B. J. Nelson, B. Scassellati, M. Taddeo, R. Taylor, M. Veloso, Z. L. Wang, R. Wood, The grand challenges of science robotics. *Sci. Robot.* **3**, eaar7650 (2018).
3. M. Runciman, A. Darzi, G. P. Mylonas, Soft robotics in minimally invasive surgery. *Soft Robot.* **6**, 423–443 (2019).
4. H. Rafii-Tari, C. J. Payne, G.-Z. Yang, Current and emerging robot-assisted endovascular catheterization technologies: A review. *Ann. Biomed. Eng.* **42**, 697–715 (2014).
5. J. Burgner-Kahrs, D. C. Rucker, H. Choset, Continuum robots for medical applications: A survey. *IEEE Trans. Robot.* **31**, 1261–1280 (2015).
6. S. A. Menaker, S. S. Shah, B. M. Snelling, S. Sur, R. M. Starke, E. C. Peterson, Current applications and future perspectives of robotics in cerebrovascular and endovascular neurosurgery. *J. Neurointerv. Surg.* **10**, 78–82 (2018).
7. D. B. Camarillo, C. R. Carlson, J. K. Salisbury, Configuration tracking for continuum manipulators with coupled tendon drive. *IEEE Trans. Robot.* **25**, 798–808 (2009).
8. M. Mahvash, P. E. Dupont, Stiffness control of surgical continuum manipulators. *IEEE Trans. Robot.* **27**, 334–345 (2011).
9. T. Kato, I. Okumura, S.-E. Song, A. J. Golby, N. Hata, Tendon-driven continuum robot for endoscopic surgery: Preclinical development and validation of a tension propagation model. *IEEE/ASME Trans. Mechatron.* **20**, 2252–2263 (2015).
10. M. M. Dalvand, S. Nahavandi, R. D. Howe, An analytical loading model for *n*-tendon continuum robots. *IEEE Trans. Robot.* **34**, 1215–1225 (2018).
11. Y.-H. Kim, Y.-J. Park, H. In, C. W. Jeong, K.-J. Cho, Design concept of hybrid instrument for laparoscopic surgery and its verification using scale model test. *IEEE/ASME Trans. Mechatron.* **21**, 142–153 (2016).
12. Z. Li, L. Wu, H. Ren, H. Yu, Kinematic comparison of surgical tendon-driven manipulators and concentric tube manipulators. *Mech. Mach. Theory* **107**, 148–165 (2017).
13. Y. Hu, W. Li, L. Zhang, G.-Z. Yang, Designing, prototyping, and testing a flexible suturing robot for transanal endoscopic microsurgery. *IEEE Robot. Autom. Lett.* **4**, 1669–1675 (2019).
14. J. Bonatti, G. Vetrovec, C. Riga, O. Wazni, P. Stadler, Robotic technology in cardiovascular medicine. *Nat. Rev. Cardiol.* **11**, 266–275 (2014).
15. M. P. Armacost, J. Adair, T. Munger, R. R. Viswanathan, F. M. Creighton, D. T. Crud, R. Sehra, Accurate and reproducible target navigation with the Stereotaxis Niobe® magnetic navigation system. *J. Cardiovasc. Electrophysiol.* **18**, S26–S31 (2007).
16. V. N. T. Le, N. H. Nguyen, K. Alameh, R. Weerasooriya, P. Pratten, Accurate modeling and positioning of a magnetically controlled catheter tip. *Med. Phys.* **43**, 650–663 (2016).
17. J. Edelmann, A. J. Petruska, B. J. Nelson, Magnetic control of continuum devices. *Int. J. Rob. Res.* **36**, 68–85 (2017).
18. C. Chautems, S. Lyttle, Q. Boehler, B. J. Nelson, Design and evaluation of a steerable magnetic sheath for cardiac ablations. *IEEE Robot. Autom. Lett.* **3**, 2123–2128 (2018).
19. J. Edelmann, A. J. Petruska, B. J. Nelson, Estimation-based control of a magnetic endoscope without device localization. *J. Med. Robot. Res.* **03**, 1850002 (2018).
20. A. K. Hoshiar, S. Jeon, K. Kim, S. Lee, J.-Y. Kim, H. Choi, Steering algorithm for a flexible microrobot to enhance guidewire control in a coronary angioplasty application. *Micromachines* **9**, 617 (2018).
21. S. Jeon, A. K. Hoshiar, K. Kim, S. Lee, E. Kim, S. Lee, J.-y. Kim, B. J. Nelson, H.-J. Cha, B.-J. Yi, H. Choi, A magnetically controlled soft microrobot steering a guidewire in a three-dimensional phantom vascular network. *Soft Robot.* **6**, 54–68 (2019).
22. U.S. Food and Drug Administration (FDA), Class 2 medical device recalls: Cronus endovascular guidewires (510(K) Number: K021363, FDA, 2004); https://www.accessdata.fda.gov/scripts/cdrh/cfdocs/cfRES/res.cfm?start_search=1&knumber=K021363.
23. C. Laschi, B. Mazzolai, M. Cianchetti, Soft robotics: Technologies and systems pushing the boundaries of robot abilities. *Sci. Robot.* **1**, eaah3690 (2016).
24. M. Sitti, Miniature soft robots — Road to the clinic. *Nat. Rev. Mater.* **3**, 74–75 (2018).
25. S. I. Rich, R. J. Wood, C. Majidi, Untethered soft robotics. *Nat. Electron.* **1**, 102–112 (2018).
26. J. T. B. Overvelde, T. Kloek, J. J. A. D'haen, K. Bertoldi, Amplifying the response of soft actuators by harnessing snap-through instabilities. *Proc. Natl. Acad. Sci. U.S.A.* **112**, 10863–10868 (2015).
27. T. Ranzani, S. Russo, N. W. Bartlett, M. Wehner, R. J. Wood, Increasing the dimensionality of soft microstructures through injection-induced self-folding. *Adv. Mater.* **30**, 1802739 (2018).
28. G. Z. Lum, Z. Ye, X. Dong, H. Marvi, O. Erin, W. Hu, M. Sitti, Shape-programmable magnetic soft matter. *Proc. Natl. Acad. Sci. U.S.A.* **113**, E6007–E6015 (2016).
29. W. Hu, G. Z. Lum, M. Mastrangeli, M. Sitti, Small-scale soft-bodied robot with multimodal locomotion. *Nature* **554**, 81–85 (2018).
30. Y. Kim, H. Yuk, R. Zhao, S. A. Chester, X. Zhao, Printing ferromagnetic domains for untethered fast-transforming soft materials. *Nature* **558**, 274–279 (2018).
31. R. Zhao, Y. Kim, S. A. Chester, P. Sharma, X. Zhao, Mechanics of hard-magnetic soft materials. *J. Mech. Phys. Solids* **124**, 244–263 (2019).
32. Y. Fu, H. Liu, W. Huang, S. Wang, Z. Liang, Steerable catheters in minimally invasive vascular surgery. *Int. J. Med. Robot. Comp.* **5**, 381–391 (2009).
33. X. Yu, H. Yuk, G. A. Parada, Y. Wu, X. Liu, C. S. Nabzdyk, K. Youcef-Toumi, J. Zang, X. Zhao, Multifunctional "hydrogel skins" on diverse polymers with arbitrary shapes. *Adv. Mater.* **31**, 1807101 (2019).
34. M. Mooney, The viscosity of a concentrated suspension of spherical particles. *J. Colloid Sci.* **6**, 162–170 (1951).
35. S. Ahmed, F. R. Jones, A review of particulate reinforcement theories for polymer composites. *J. Mater. Sci.* **25**, 4933–4942 (1990).
36. T. Krings, J. Finney, P. Niggemann, P. Reinacher, N. Lück, A. Drexler, J. Lovell, A. Meyer, R. Sehra, P. Schauerte, M. Reinges, F. J. Hans, A. Thron, Magnetic versus manual guidewire manipulation in neuroradiology: In vitro results. *Neuroradiology* **48**, 394–401 (2006).
37. T. E. Darsaut, V. Costalat, I. Salazkin, S. Jamali, F. Berthelet, G. Gevry, D. Roy, J. Raymond, Fatal avulsion of choroidal or perforating arteries by guidewires: Case reports, ex vivo experiments, potential mechanisms and prevention. *Interv. Neuroradiol.* **20**, 251–260 (2014).
38. C. R. Pasarikovski, J. Cardinell, V. X. D. Yang, Perspective review on applications of optics in cerebral endovascular neurosurgery. *J. Biomed. Opt.* **24**, 1–7 (2019).
39. K. P. Rajan, A. Al-Ghamdi, R. Parameswar, G. B. Nando, Blends of thermoplastic polyurethane and polydimethylsiloxane rubber: Assessment of biocompatibility and suture holding strength of membranes. *Int. J. Biomater.* **2013**, 240631 (2013).
40. F. Wang, X. Yong, J. Deng, Y. Wu, Poly(*N,N*-dimethylacrylamide-octadecyl acrylate)-clay hydrogels with high mechanical properties and shape memory ability. *RSC Adv.* **8**, 16773–16780 (2018).
41. L. Weng, A. Gouldstone, Y. Wu, W. Chen, Mechanically strong double network photocrosslinked hydrogels from *N,N*-dimethylacrylamide and glycidyl methacrylated hyaluronan. *Biomaterials* **29**, 2153–2163 (2008).
42. V. E. Donohue, F. McDonald, R. Evans, In vitro cytotoxicity testing of neodymium-iron-boron magnets. *J. Appl. Biomater.* **6**, 69–74 (1995).
43. M. Hopp, S. Rogaschewski, T. Groth, Testing the cytotoxicity of metal alloys used as magnetic prosthetic devices. *J. Mater. Sci. Mater. Med.* **14**, 335–345 (2003).
44. L. Calabrese, A. Caprì, F. Fabiano, L. Bonaccorsi, C. Borsellino, E. Proverbio, Corrosion behaviour of a silane protective coating for NdFeB magnets in dentistry. *Int. J. Corros.* **2015**, 345038 (2015).

45. P. Saravanapavan, J. E. Gough, J. R. Jones, L. L. Hench, Antimicrobial macroporous gel-glasses: Dissolution and cytotoxicity. *Key Eng. Mater.* **254-256**, 1087–1090 (2004).

46. J. K. M. F. Daguano, S. O. Rogero, M. C. Crovace, O. Peitl, K. Strecker, C. dos Santos, Bioactivity and cytotoxicity of glass and glass–ceramics based on the 3CaO·P₂O₅–SiO₂–MgO system. *J. Mater. Sci. Mater. Med.* **24**, 2171–2180 (2013).

47. B. L. Nguyen, J. L. Merino, E. S. Gang, Remote navigation for ablation procedures—A new step forward in the treatment of cardiac arrhythmias. *Eur. Cardiol.* **6**, 50–56 (2010).

48. M. P. Kummer, J. J. Abbott, B. E. Kratochvil, R. Borer, A. Sengul, B. J. Nelson, Octomag: An electromagnetic system for 5-DOF wireless micromanipulation. *IEEE Trans. Robot.* **26**, 1006–1017 (2010).

49. E. Diller, J. Giltinan, M. Sitti, Independent control of multiple magnetic microrobots in three dimensions. *Int. J. Robot. Res.* **32**, 614–631 (2013).

50. A. J. Petruska, J. J. Abbott, Omnimagnet: An omnidirectional electromagnet for controlled dipole-field generation. *IEEE Trans. Magn.* **50**, 8400810 (2014).

51. L. B. Kratchman, T. L. Bruns, J. J. Abbott, R. J. Webster, Guiding elastic rods with a robot-manipulated magnet for medical applications. *IEEE Trans. Robot.* **33**, 227–233 (2017).

52. J. Rahmer, C. Stehning, B. Gleich, Spatially selective remote magnetic actuation of identical helical micromachines. *Sci. Robot.* **2**, eaal2845 (2017).

53. C. R. Thornley, L. N. Pham, J. J. Abbott, Reconsidering six-degree-of-freedom magnetic actuation across scales. *IEEE Robot. Autom. Lett.* **4**, 2325–2332 (2019).

54. G. A. Parada, H. Yuk, X. Liu, A. J. Hsieh, X. Zhao, Impermeable robust hydrogels via hybrid lamination. *Adv. Healthc. Mater.* **6**, 1700520 (2017).

55. G. A. Holzapfel, in *Nonlinear Solid Mechanics: A Continuum Approach for Engineering* (Wiley, 2000) pp. 205–227.

56. G. A. Holzapfel, in *Nonlinear Solid Mechanics: A Continuum Approach for Engineering* (Wiley, 2000) pp. 141–152.

Citation: Y. Kim, G. A. Parada, S. Liu, X. Zhao, Ferromagnetic soft continuum robots. *Sci. Robot.* **4**, eaax7329 (2019).

Science Robotics

Ferromagnetic soft continuum robots

Yoonho Kim, German A. Parada, Shengduo Liu and Xuanhe Zhao

ARTICLE TOOLS	http://robotics.sciencemag.org/content/4/33/eaax7329
SUPPLEMENTARY MATERIALS	http://robotics.sciencemag.org/content/suppl/2019/08/23/4.33.eaax7329.DC1
REFERENCES	This article cites 53 articles, 3 of which you can access for free http://robotics.sciencemag.org/content/4/33/eaax7329#BIBL
PERMISSIONS	http://www.sciencemag.org/help/reprints-and-permissions

Supplementary Materials for

Ferromagnetic soft continuum robots

Yoonho Kim, German A. Parada, Shengduo Liu, Xuanhe Zhao*

*Corresponding author. Email: zhaox@mit.edu

The PDF file includes:

Other Supplementary Material for this manuscript includes the following:

Movie S4 (.mp4 format). Demonstration of the ferromagnetic soft continuum robot with hydrogel skin (the same prototype presented in movie S3) navigating through a 3D cerebrovascular phantom (the circle of Willis model with multiple aneurysms).

Movie S5 (.mp4 format). Comparison of the navigating performance of the ferromagnetic soft continuum robot with (left) and without (right) hydrogel skin as a lubricating layer on the robots' surface in the same experimental setup presented in movie S4.

Movie S6 (.mp4 format). Comparison of the navigating performance of the ferromagnetic soft continuum robot with hydrogel skin (left) and a commercial hydrophilic guidewire with a preshaped tip (right).

Movie S7 (.mp4 format). Demonstration of the capability of steerable laser delivery with the ferromagnetic soft continuum robot with a concentric optical fiber incorporated as a functional core.

Movie S8 (.mp4 format). Demonstration of steerable laser delivery in the carotid artery of the vascular phantom model presented in movie S4.

Text

Analytical model for ferromagnetic soft continuum robots

We denote the magnetic moment density (or magnetization) at any point of a ferromagnetic soft material in the undeformed, reference configuration by a vector $\mathbf{M}$. Under an applied magnetic field, denoted by a vector $\mathbf{B}$, the ferromagnetic soft material can deform (**Fig. 3A**). The deformation at any point of the material is characterized by the deformation gradient tensor $\mathbf{F}$. The application of the magnetic field on the embedded magnetic moment in the material generates the magnetic Cauchy stress that drives its deformation. Meanwhile, the deformation of the material generates the elastic Cauchy stress. For incompressible solids, the magnetic Cauchy stress can be expressed as (*31, 32*)

$$\boldsymbol{\sigma}^{\mathrm{magnetic}} = -\mathbf{B} \otimes \mathbf{FM}\,, \tag{S1}$$

where the operator $\otimes$ denotes the dyadic product, which takes two vectors to yield a second-order tensor. If adopting the incompressible neo-Hookean model among existing hyperelastic constitutive models (*47*), the elastic Cauchy stress $\boldsymbol{\sigma}^{\mathrm{elastic}}$ can be expressed as

$$\boldsymbol{\sigma}^{\mathrm{elastic}} = G\mathbf{F}\mathbf{F}^{\mathrm{T}} - p\mathbf{1}\,, \tag{S2}$$

where G is the shear modulus, $\mathbf{F}^{\mathrm{T}}$ is the transpose of $\mathbf{F}$, $\mathbf{1}$ is the identity tensor, and p is the hydrostatic pressure that needs to be determined from boundary conditions (*47*). Assuming a quasi-static process where the inertial effects are negligible, the total Cauchy stress $\boldsymbol{\sigma} = \boldsymbol{\sigma}^{\mathrm{elastic}} + \boldsymbol{\sigma}^{\mathrm{magnetic}}$ can then be substituted into the following equilibrium equation:

$$\mathrm{div}\boldsymbol{\sigma} + \mathbf{b} = \mathbf{0}\,, \tag{S3}$$

where div denotes the divergence, and $\mathbf{b}$ denotes the body force (e.g., gravitational) per unit volume. This equilibrium equation can be solved to calculate the deformation gradient $\mathbf{F}$, thereby finding the equilibrium configuration of the ferromagnetic soft material under magnetic actuation. While alternate approaches based on magnetic forces and torques have been developed to calculate the deformation of ferromagnetic soft materials (*29, 30*), the current approach based on magnetic stress can be readily implemented in commercial finite-element software packages such as Abaqus.

For the magnetically responsive tip of the ferromagnetic soft continuum robot, the gravitational body force can be neglected due to the considerably greater contribution from the magnetic stress. For small bending, where the deflection of the free end is below 10% of the length, i.e. $\delta\,/\,L \leq 0.1$, a tractable analytical expression can be derived for quantitative prediction of the degree of deflection. When a uniform magnetic field $\mathbf{B}$ is applied perpendicularly to the magnetically responsive tip with magnetization $\mathbf{M}$ along the axial direction (**Fig. 3A**), the only non-zero, shear stress component of the magnetic Cauchy stress tensor in the reference (undeformed) configuration

(i.e. $\mathbf{F} = \mathbf{1}$) can be calculated from Eq. (S1) to be $\sigma^{\text{magnetic}} = -MB$ as a scalar quantity. This shear stress gives rise to magnetic moment $T = -MBAL$ across the body, where A denotes the cross-sectional area ($A = \pi D^2 / 4$) of the circular beam of length L and diameter D. Equivalently, this magnetic moment can be considered to be generating a point force $F = MBA$ at the free end of the beam along the applied field direction (as illustrated in the schematic in **Fig. 3G**). The bending stiffness of a beam can be expressed as $K_b = 3EI / L^3$, where E denotes the Young's modulus of the constituent material, and I denotes the area moment of inertia, which can be expressed as $I = \pi D^4 / 64$ for a circular beam of diameter D. Then, the deflection of the free end of the beam, denoted δ, under this point force can be analytically expressed for small deflection case as

$$\delta = \frac{F}{K_b} = \frac{16MBL^3}{3ED^2}. \tag{S4}$$

For incompressible solids, for which $E = 3G$, Eq. (S4) can be expressed in a normalized from as

$$\frac{\delta}{L} = \frac{16}{9}\left(\frac{MB}{G}\right)\left(\frac{L}{D}\right)^2, \tag{S5}$$

which is identical to Eq. (1) introduced in the main text. From this analytical expression, it becomes evident that the normalized deflection of the magnetically responsive tip of the ferromagnetic soft continuum robot under magnetic actuation is determined by the two dimensionless factors: MB / G and L / D. The former can be interpreted as the applied field strength B normalized by the material properties M and G, while the latter is the aspect ratio, a geometric factor that can largely affect the bending stiffness of the beam. Also, the work done by the equivalent point force F while deforming the beam by small deflection δ, can be expressed as

$$W = F\delta = \frac{4\pi}{9}\left(\frac{M^2B^2}{G}\right)L^3. \tag{S6}$$

When divided by the volume, Eq. (S6) leads to the following expression for the energy density:

$$u = \frac{16}{9}\left(\frac{M^2B^2}{G}\right)\left(\frac{L}{D}\right)^2, \tag{S7}$$

which is identical to Eq. (4) introduced in the main text. Here, it is assumed that no energy is dissipated during the deformation, based on the underlying assumption of hyperelastic solids (*46*).

Alternative model based on magnetic body force and torque

As discussed in the previous section, the current model for ferromagnetic soft materials is based on the magnetic Cauchy stress and the total Cauchy stress. Since the traditional approaches are commonly based on the magnetic body force and torque and the elastic Cauchy stress (28, 29), here we describe how the magnetic Cauchy stress presented in Eq. (S1) is related to the magnetic body force and torque in the following paragraphs.

Under the assumption of *ideal hard-magnetic soft materials* (*31*), which holds for the proposed ferromagnetic soft continuum robots, the magnetization vector **M** can be considered independent of the externally applied magnetic field **B**, provided that the materials are magnetically saturated and that the applied field strength is far below the coercivity, at which the reversal of remnant magnetization takes place.

For an incompressible ideal hard-magnetic soft material, the magnetic body torque per unit volume of the material (i.e. magnetic body torque density) generated by the external field **B** applied to the magnetization **M** can be expressed as a consequence of the angular momentum balance (*31, 47*) as

$$\boldsymbol{\tau}^{\text{magnetic}} = -\boldsymbol{\mathcal{E}} : (\boldsymbol{\sigma}^{\text{magnetic}})^{\text{T}} = \mathbf{FM} \times \mathbf{B}, \tag{S8}$$

where $\boldsymbol{\mathcal{E}} = \varepsilon_{ijk} \mathbf{e}_i \otimes \mathbf{e}_j \otimes \mathbf{e}_k$ is the third-order permutation tensor; the operator **:** denotes the double contraction of two tensors; and **FM** accounts for the reoriented magnetization vector in the current (deformed) configuration. Also, the magnetic body force acting on the material per unit volume (i.e. magnetic body force density) under the applied magnetic field **B** can be expressed from Eqs. (S1) and (S3) as

$$\mathbf{b}^{\text{magnetic}} = -\text{div}\boldsymbol{\sigma}^{\text{magnetic}} = (\text{grad}\mathbf{B})\mathbf{FM}, \tag{S9}$$

where $\text{grad}\mathbf{B}$ denotes the spatial gradient of the applied magnetic field, which gives rise to the magnetic body force. Again, **FM** represents the reoriented magnetization vector in the current (deformed) configuration. Note that the magnetic body torque and force densities in Eqs. (S8) and (S9) are consistent with their common expressions used elsewhere in the literature (*18, 19, 29, 45*).

As shown above, our approach based on the magnetic Cauchy stress enables the magnetic body torques and forces to be treated as stresses when solving the equilibrium equations to find the final configuration of the ferromagnetic soft continuum robots under external magnetic fields. When the magnetic body torque and force (instead of the magnetic Cauchy stress) are directly employed to calculate the deformation, the elastic Cauchy stress (instead of the total Cauchy stress) can be used in the equilibrium equations. While the models based on the magnetic Cauchy stress or the magnetic body torque and force will reach the same deformation, the current approach based on the magnetic Cauchy stress can be readily implemented in commercial finite-element software packages such as Abaqus and hence enables accurate and quantitative prediction of the final configuration of the robot under given conditions and geometries.

Magnetic actuation and steering with a cylindrical permanent magnet

In this paper, a cylindrical NdFeB magnet (DY0Y0-N52, K&J Magnetic, Inc.) is employed to demonstrate the magnetic steering function of the proposed ferromagnetic soft continuum robot. The radius (25 mm) and height (50 mm) of the cylindrical magnet are denoted as R and H, respectively (**fig. S5A**). The basic principle behind the magnetic steering is to align the central axis of the magnet along a desired direction to induce the bending actuation on the robot's magnetically responsive tip towards the along the desired direction (**fig. S5B**). The degree of bending, which is determined by the applied field strength, is controlled by adjusting the distance between the magnet and the robot. The magnetic field strength along the central axis of the magnet can be expressed as a function of distance from the surface (denoted z in **fig. S5A**) as

$$B_z(0,0,z) = \frac{B_0 \sqrt{R^2 + H^2}}{H} \left(\frac{z+H}{\sqrt{(z+H)^2 + R^2}} - \frac{z}{\sqrt{z^2 + R^2}} \right), \tag{S10}$$

where B_0 denotes the surface field strength, which is 662 mT for the specific magnet used. Typical working distance for the set of demonstrations presented in the paper ranges from around 40 to 80 mm, which corresponds to the field strength ranging from around 20 to 80 mT, according to Eq. (S8). As discussed earlier, under spatially uniform magnetic fields, the bending actuation of the ferromagnetic soft continuum robot is driven by magnetic body torques generated from the embedded magnetic particles. However, when the applied actuating field is spatially non-uniform, which is the case when a single permanent magnet is used for actuation, magnetic body force does exist and can contribute to the magnetic steering and control of the robot.

Influence of a field gradient on the magnetic actuation and steering

When the magnet used for actuation is sufficiently larger than the segment of robot being actuated, we may neglect the nonlinear edge effects and further assume that the magnetic fields are almost parallel and that their spatial gradients are dominant along the central axis (z-direction) in terms of the magnitude, as illustrated in **fig. S6**. Then, the field gradient along the central axis of the cylindrical magnet discussed above can be obtained from Eq. (S10) as

$$\frac{\partial B_z}{\partial z} = \frac{B_0 \sqrt{R^2 + H^2}}{H} \left(\frac{1}{\sqrt{(z+H)^2 + R^2}} - \frac{1}{\sqrt{z^2 + R^2}} + \frac{z^2}{(z^2 + R^2)^{3/2}} - \frac{(z+H)^2}{((z+H)^2 + R^2)^{3/2}} \right). \tag{S11}$$

This gives the gradient values ranging from around 0.5 to 4 mT/mm over the range of typical working distance (40-80 mm) mentioned above. Under this range of field gradients, the magnetic body force per unit volume can be estimated from Eq. (S9) to be on the order of 64 to 512 kN/m³, when assuming that the robot's tip is aligned with the central axis of the magnet as illustrated in **fig. S6**. Compared to this, the gravitational body force per unit volume is calculated to be on the order of 23 kN/m³ for ferromagnetic soft composite based on PDMS + NdFeB (20 vol%), whose mass

density is 2.273 g/cm^3. This means that the field gradient along the central axis of the magnet is generating sufficient magnetic body forces in the deformed configuration to maintain the robot's deflected tip, as illustrated in **fig. S6**.

As Eq. (S9) implies, however, the magnetic body force varies with the configuration, or more specifically, the alignment between the robot's magnetization and the external field. In the reference configuration in **fig. S6**, in which the external field is being applied perpendicularly to the magnetization vector, the magnetic body force acting along the magnet's central axis is considered to be almost negligible. As the body deforms and the robot's magnetization becomes more aligned with the central axis of the magnet, the magnetic body force increases. Therefore, we can conclude that, when the robot is actuated and controlled with a magnet, the bending actuation in general is initiated and driven by the magnetic body torque and then facilitated and further supported by the magnetic body force as the robot's body deforms. We therefore can also conclude that utilizing spatial gradients to exploit magnetic body forces for bending actuation can be a good strategy to more effectively control the robot's configurations, as demonstrated in the series of functional tasks presented in this paper.

Supplementary Figures
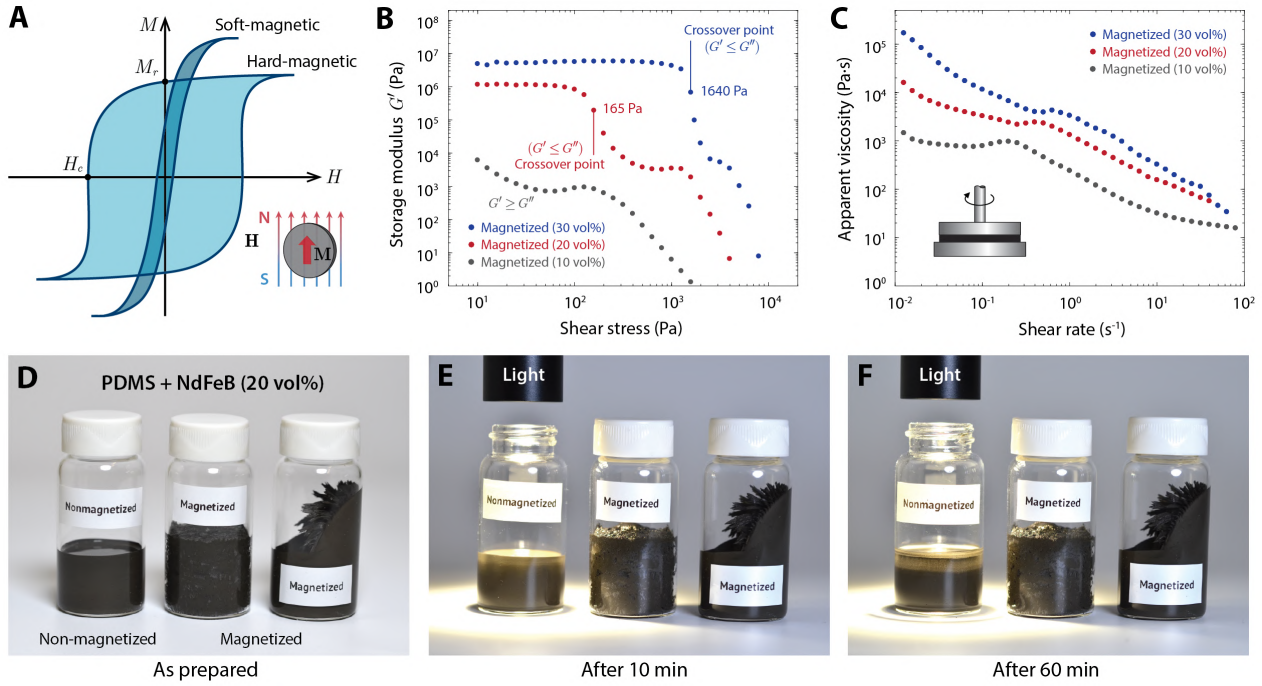
Fig. S1. Rheological properties of ferromagnetic composite inks. (**A**) Magnetization curves with magnetic hysteresis loops of soft-magnetic and hard-magnetic materials, both of which are ferromagnetic and thus develop strong induced magnetization M when exposed to an external magnetizing field H. Soft-magnetic materials form a sharp and narrow hysteresis curve due to the low coercivity H_c and hence do not sustain high remnant magnetization M_r independently of external fields. Hard-magnetic materials exhibit much higher coercivity and thus can retain high remnant magnetization unless a strong demagnetizing field beyond the coercivity is applied. (**B**) Storage modulus plotted against the applied shear stress for permanently magnetized composite inks with 10 vol% (grey), 20 vol% (red), and 30 vol% (blue) of NdFeB dispersed in uncured PDMS resin. The crossover point at which the storage modulus G' becomes smaller than the loss modulus G'' defines the shear yield stress beyond which the magnetized composite paste can flow. The identified shear yield stresses for 20 vol% and 30 vol% inks are 165 kPa and 1640 kPa, respectively. The shear yield stress for 10 vol% ink is smaller than the lower bound of the applied shear stress, and hence the data shows that the ink is already fluidized due to the applied shear stress. (**C**) Apparent viscosity plotted against the applied shear rate for 10 vol% (grey), 20 vol% (red), and 30 vol% (blue) inks. The data reveals shear-thinning behavior of the thixotropic paste of magnetized ferromagnetic composite ink. (**D-F**) The presence of shear yield stresses in 20 vol% magnetized inks helps preventing their phase separation due to gravitational sedimentation of the dispersed particles over time. The vial on the left contains nonmagnetized, freely flowing composite ink. In the middle, already magnetized composite ink is contained. On the right, nonmagnetized ink is first loaded and then magnetized while being contained in the vial.
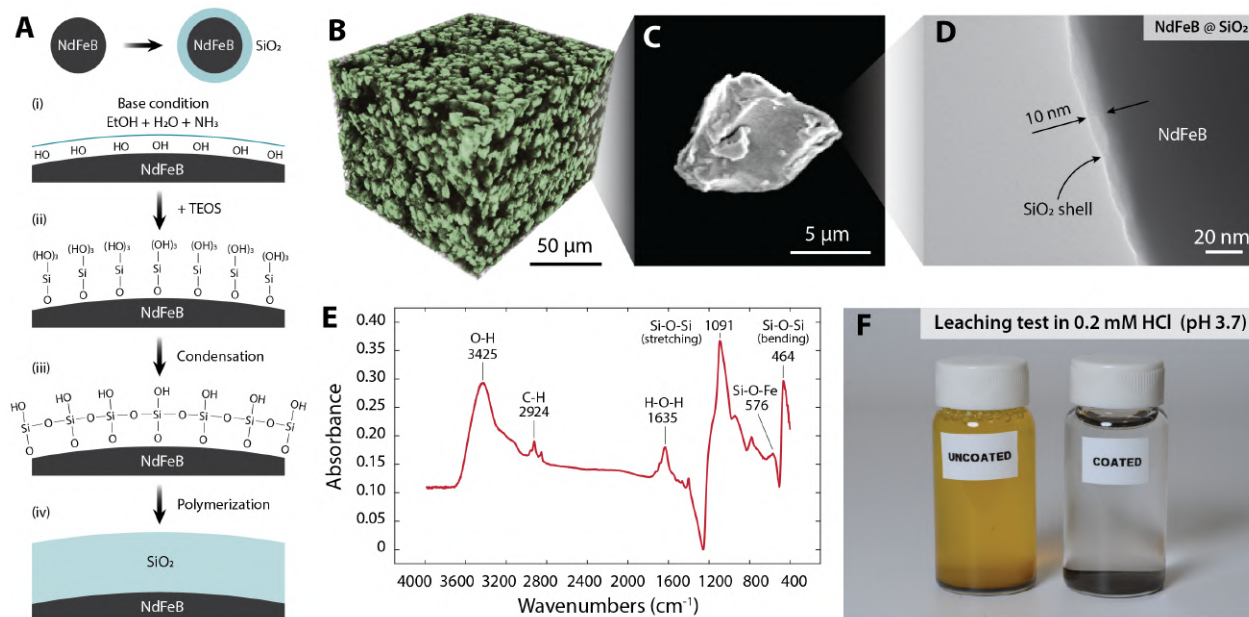
Fig. S2. Characterizations of silica-coated magnetic particles. (**A**) Schematic of the polycondensation reaction of TEOS in the presence of catalysts in basic conditions. The nucleation and polymerization of TEOS lead to crosslinked layer of silica around the NdFeB particles. (**B**) Micro-computed tomography image of solidified ferromagnetic composite based on PDMS and silica-coated NdFeB particles showing uniformly dispersed particles with no obvious gradient due to sedimentation. (**C**) Scanning electron microscope image of silica-coated NdFeB particles indicating the size of a single particle. (**D**) Transmission electron microscope image of a silica-coated NdFeB particle, from which the thickness of the silica layer is identified to be 10 nm. (**E**) Fourier transform infrared spectroscopy of silica-coated NdFeB particles clearly indicating the presence of Si-O-Si bonds. (**F**) Leaching test of both uncoated and coated NdFeB particles in 0.2 mM HCl solution (pH 3.7) for 3 days. No visible change was observed in the silica-coated particles owing to the presence of the protective silica layer, whereas the uncoated particles were highly oxidized, turning the color of the solution yellow.
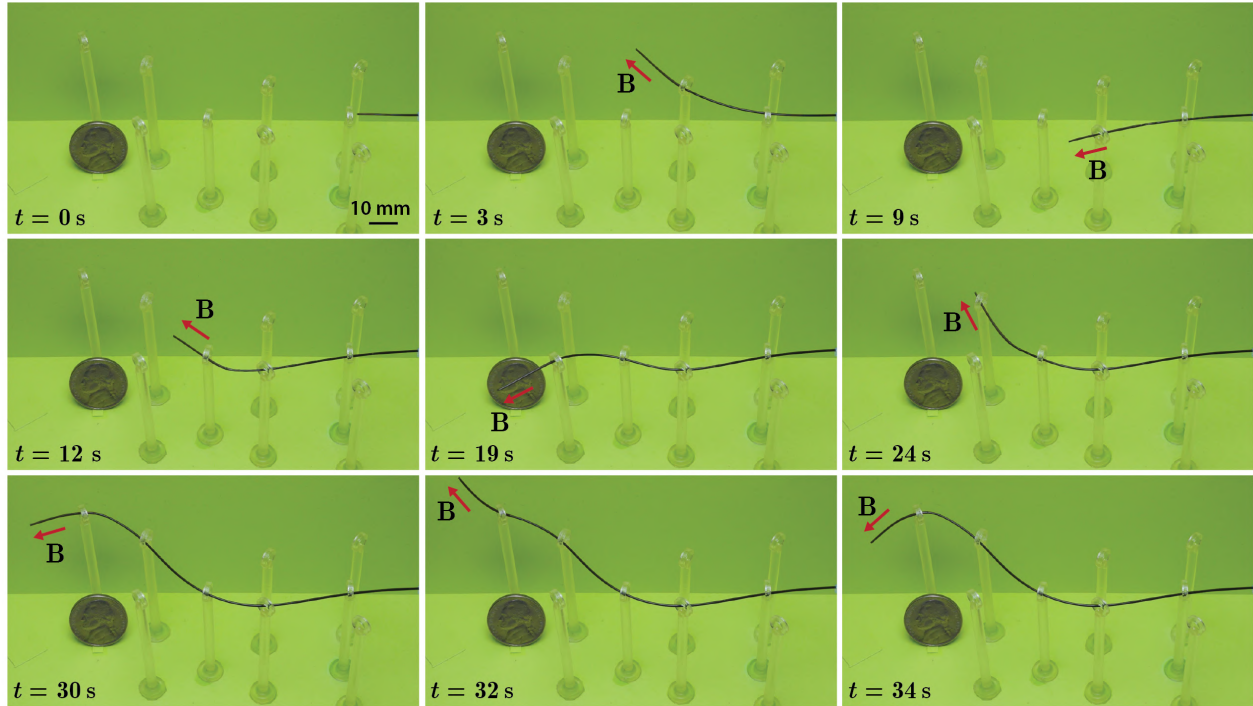
Fig. S3. Experimental demonstration of active steering and navigating capabilities with a TPU-based prototype. A printed TPU+NdFeB (30 vol%) segment connected to a commercial guidewire selectively navigates through a set of rings based on magnetic actuation and steering. The magnetic fields for actuation (20 to 80 mT) are generated by a cylindrical permanent magnet (diameter and height of 50 mm) at distance (40 to 80 mm). The proximal end of the guidewire is pushed to advance the magnetically steerable distal tip of the robot during the navigation. The outer diameter of the demonstrated prototype is 810 µm.

Fig. S4. Experimental setups and dimensions for the demonstrations of active steering and navigating capabilities of ferromagnetic soft continuum robots based on magnetic actuation. (**A**) A set of rings loosely placed at different locations (in mm) with different heights (in mm) and tilt angles, through which the prototypes presented in **Fig. 4**, **fig. S3**, **Movies S1** and **S2** navigate selectively based on the demonstrated active steering capabilities. (**B**) A set of rings tightly placed to form a tortuous path, which is navigated by the prototype presented in **Fig. 5** and **Movie S3**.

Fig. S5. Magnetic actuation and steering mechanism based on a cylindrical permanent magnet for experimental demonstrations of the proposed ferromagnetic soft continuum robots. (**A**) Schematic of a cylindrical magnet of radius R and height H and the magnetic field around the magnet. (**B**) Basic principle for magnetic actuation and steering of the ferromagnetic soft continuum robot employed in the experimental demonstrations presented in the paper. The central axis of the magnet is aligned along the desired direction to induce the bending actuation on the robot's magnetically responsive tip towards the along the desired direction. The degree of bending, which is determined by the applied field strength, is controlled by adjusting the distance between the magnet and the robot.
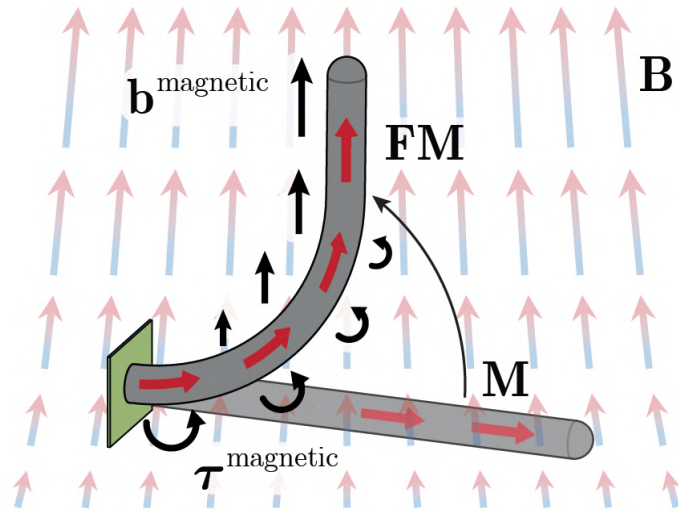
Fig. S6. Influence of spatial gradients of the actuating magnetic field on the actuation and steering of the ferromagnetic soft continuum robot. In the reference configuration, the magnetic field **B** generated along the central axis of a large cylindrical magnet is applied perpendicularly to the magnetization vector **M** along the body, which gives rise to magnetic body torques (τ^{magnetic}) that drive the bending actuation. As the body deforms under the applied field with spatial gradients along the field direction, magnetic body forces ($\mathbf{b}^{\text{magnetic}}$) are generated. As the magnetization in the current configuration **FM** becomes more aligned with the applied field direction, the magnetic body force increases whereas the magnetic body torque decreases. This means that, when the robot is actuated and controlled with a magnet, the bending actuation is initiated and driven by the magnetic body torque and then further supported by the magnetic body force as the robot's body deforms.
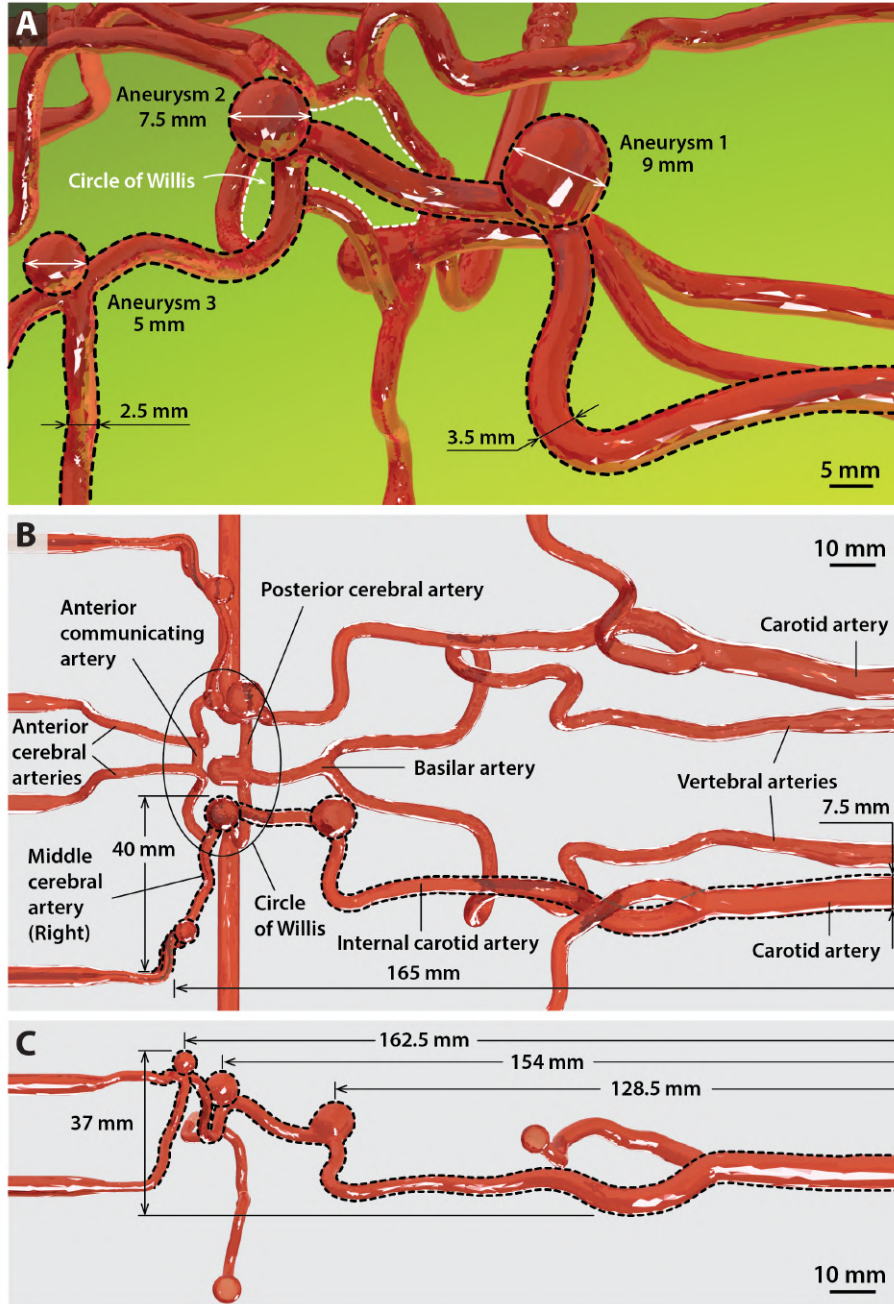
Fig. S7. Dimensions and details of the cerebrovascular phantom model used for the experimental demonstration of the active steering and navigating capabilities of the proposed ferromagnetic soft continuum robot. (A) Detailed view and relevant dimensions of the vascular structure of the phantom model around a particular cerebrovascular anatomy, called the circle of Willis, as well as the surrounding arteries with multiple aneurysms. The path that is navigated by the prototype presented in **Fig. 6** and **Movie S4**, from the carotid artery to the right middle cerebral artery, is indicated with dashed lines. (B) The vascular anatomy and dimension of the real-sized phantom model (top view) used in the experimental demonstration of the proposed ferromagnetic soft continuum robot. (C) The vascular structure and dimension of the phantom model (side view) around the path.

Supporting Movies

Movie S1. Demonstration of the ferromagnetic soft continuum robot actively steering and selectively navigating through a set of rings based on magnetic actuation. The demonstrated prototype is fabricated through the injection modeling process based on PDMS+NdFeB (20 vol%) composite to contain a nitinol core for additional mechanical support. The magnetic fields for actuation (20 to 80 mT) are generated by a cylindrical permanent magnet (diameter and height of 50 mm) at distance (40 to 80 mm). The magnetic steering is controlled by manually manipulating the magnet's position and orientation, according to the actuation and steering mechanism described in **fig. S5B**. The proximal end is pushed to advance the magnetically steered distal end of the robot during the navigation. The outer diameter of the demonstrated prototype is 600 µm. The average time taken to complete the given tasks is measured to be 50 ± 1.58 s from 5 trials.

Movie S2. Demonstration of the ferromagnetic soft continuum robot based on TPU + NdFeB (30 vol%) composite in the same experimental setup presented in **Movie S1**. The demonstrated prototype is fabricated by connecting a printed TPU composite segment to a commercial guidewire with a TPU polymer and a tapered nitinol wire. The magnetic fields for actuation (20 to 80 mT) are generated by a cylindrical permanent magnet (diameter and height of 50 mm) at distance (40 to 80 mm). The magnetic steering is controlled by manually manipulating the magnet's position and orientation, according to the actuation and steering mechanism described in the manuscript. The proximal end is pushed to advance the magnetically steered distal end of the robot during the navigation. The outer diameter of the demonstrated prototype is 810 µm to ensure sufficient mechanical stiffness required to perform the demonstrated tasks. The average time taken to complete the given tasks is measured to be 54 ± 1.87 s from 5 trials.

Movie S3. Demonstration of the ferromagnetic soft continuum robot navigating through a highly nonlinear path formed by a set of tightly spaced multiple rings, based on multiple modes and degrees of deflection upon magnetic actuation. The demonstrated prototype is fabricated through the injection modeling process based on PDMS+NdFeB (20 vol%) composite. The distal tip (3-mm) of the prototype is composed of the PDMS composite only, whereas the remainder contains a stiff nitinol core for additional mechanical support. The magnetic fields for actuation (20 to 80 mT) are generated by a cylindrical permanent magnet (diameter and height of 50 mm) at distance (40 to 80 mm). The magnetic steering is controlled by manually manipulating the magnet's position and orientation, according to the actuation and steering mechanism described in the manuscript. The proximal end is pushed to advance the magnetically steered distal end of the robot during the navigation. The outer diameter of the demonstrated prototype is 600 µm. The average time taken to complete the given tasks is measured to be 53.8 ± 2.56 s from 5 trials.

Movie S4. Demonstration of the ferromagnetic soft continuum robot with hydrogel skin (the same prototype presented in **Movie S3**) navigating through a 3D cerebrovascular phantom (the circle of Willis model with multiple aneurysms). The required task for is to reach all the aneurysms that are present along the desired path smoothly and safely while avoiding direct contact with the inner wall of the aneurysms. The vascular phantom model is filled with a blood analogue that simulates the friction between commercial guidewires and real blood vessels. The magnetic fields for actuation (20 to 80 mT) are generated by a cylindrical permanent magnet (diameter and height of 50 mm) at distance (40 to 80 mm). The magnetic steering is controlled by manually manipulating the magnet's

position and orientation, according to the actuation and steering mechanism described in the manuscript. The proximal end is pushed to advance the magnetically steered distal end of the robot during the navigation. The outer diameter of the demonstrated prototype is 600 μm. The demonstrated continuum robot may look thicker than the actual size because of the magnifying effect of the round, thick-walled silicone vessel. The average time taken to complete the given tasks is measured to be 42.4 ± 1.87 s from 5 trials.

Movie S5. Comparison of the navigating performance of the ferromagnetic soft continuum robot with (left) and without (right) hydrogel skin as a lubricating layer on the robots' surface in the same experimental setup presented in **Movie S4**. The uncoated prototype suffers from the substantial friction acting on the robot while going through the acute-angled corners, exhibiting unwanted and unpredictable jerky movements. Despite the omnidirectional steering capability that enables the robot to orient its distal tip towards the desired direction, the significant friction does not allow the robot's body to proceed.

Movie S6. Comparison of the navigating performance of the ferromagnetic soft continuum robot with hydrogel skin (left) and a commercial hydrophilic guidewire with a preshaped tip (right). Unlike the proposed ferromagnetic soft continuum robot with active steering capabilities, the passively steered guidewire based on twisting the whole device shows limited maneuverability in highly constraining environments, such as the region near the third (smallest) aneurysm, due to the fixed curvature of the pre-shaped tip.

Movie S7. Demonstration of the capability of steerable laser delivery with the ferromagnetic soft continuum robot with a concentric optical fiber incorporated as a functional core. The laser-emitting tip of the robot accurately points the small targets (2-mm dots) with the laser beam in a desired order based on omnidirectional magnetic steering. The magnetic fields for actuation (20 to 80 mT) are generated by a cylindrical permanent magnet (diameter and height of 50 mm) at distance (40 to 80 mm).The outer diameter of the demonstrated prototype is 500 μm.

Movie S8. Demonstration of steerable laser delivery in the carotid artery of the vascular phantom model presented in **Movie S4**. The ferromagnetic soft continuum robot emits a laser beam at different targeted sites in the artery based on magnetic steering, and then navigates downstream through the internal carotid artery after turning off the laser. The magnetic fields for manipulation (20 to 50 mT) are generated by a cylindrical permanent magnet (diameter and height of 50 mm) at distance (50 to 80 mm). The outer diameter of the demonstrated prototype is 500 μm. The demonstrated continuum robot may look thicker than the actual size because of the magnifying effect of the round, thick-walled silicone vessel.